# The Locomoting State Selectively Amplifies Activity of Sensitizing Neurons in Primary Visual Cortex

Hinojosa A.J.[1,*], Kosiachkin Ye.[1,*], Dominiak S.E.[1], Evans B.D.[2] & Lagnado L.[1]

1. Sussex Neuroscience, School of Life Sciences, University of Sussex, Brighton BN1 9QG, UK
2. AI Research Group, School of Engineering and Informatics, University of Sussex, Brighton BN1 9QG, UK

*These authors contributed equally. Correspondence to ah687@sussex.ac.uk, yk348@sussex.ac.uk or l.lagnado@sussex.ac.uk.

## Abstract

Sensory processing in the cortex reflects both adaptation to external stimuli and changes in internal state. To investigate how these processes interact in layer 2/3 of mouse V1 we combined calcium imaging, optogenetics and circuit modelling. We find that locomotion preferentially increases gain in pyramidal cells (PCs) that sensitize during visual stimulation compared to those that depress. A model explains this differential modulation through three mechanisms: (i) variations in the strength of PV and SST connectivity to individual PCs, (ii) broad locomotion-dependent weakening of PC and PV synapses, and (iii) reduced SST inhibition targeting sensitizing PCs. These results demonstrate that behavioural state selectively shifts cortical computation toward distinct adaptive regimes. The apparently paradoxical combination of increased PC gain but decreased synaptic strength is consistent with a state-dependent gating mechanism that boosts signals leaving V1 while simultaneously preventing disruption of the local excitatory-inhibitory balance required for stable computation.

## Introduction

Sensory processing in the cortex is adjusted both by adaptation to the external environment and changes in the internal physiology of the animal associated with behavioural states such as attention, arousal and satiety[1-5]. The mechanisms by which external and internal variables interact within the cortical circuitry are not understood. Here we investigate this question by analyzing how the change in state associated with locomotor activity impacts adaptation in primary visual cortex (V1) of mice[6].

The dynamics of neurons in V1 reflect adaptation on multiple time-scales. In pyramidal cells (PCs), the initial excitatory response to an increase in contrast is followed by a fast (subsecond) decrease in gain reflecting depression in feedforward inputs from the LGN[7,8]. This is immediately followed by a slower phase of adaptation that varies dramatically across the PC population: while some PCs depress in response to a high-contrast stimulus others simultaneously *sensitize*[9]. PCs within layer 2/3 are not, therefore, a homogenous population: to understand gain control we must take into account variations in local inhibitory circuits in which they are embedded.

The onset of locomotion signals changes in internal state associated with attention or arousal, acting in less than a second to amplify visual responses in PCs[3,10-12]. A major driver of this increase in gain are cholinergic fibers arriving from the basal forebrain[2,13-15]. Some of these fibers make direct synaptic connections that excite interneurons expressing vasoactive intestinal peptide (VIP)[16], leading to amplification of PC responses through a VIP->SST->PC disinhibitory pathway. The majority of the cholinergic input, however, innervates V1 diffusely to modulate circuit function through extra-synaptic (muscarinic) receptors[2,13,16]. In vitro experiments have shown that M1 and M3 receptors on soma and dendrites of PCs can increase excitability while M2 receptors on axonal compartments reduce synaptic release probability[16-18]. Accounting for state-dependent changes in cortical processing therefore requires an integrated understanding of changes in both electrical activity and the strength of synaptic connections[12]. The difficulty is that modulations of synaptic strengths are very hard to quantify in awake and behaving animals: recording from connected neuron pairs remains technically challenging and is limited to anaesthetized animals in which inhibitory microcircuits are severely compromised[19-21]. Current understanding of synaptic modulation in cortical circuits is derived from *ex vivo* studies or inferred from indirect *in vivo* observations and modelling[12,22,23].

To understand how locomotion and adaptation interact in V1 of mice we used calcium imaging to record visual responses in PCs and the three major classes of interneuron (VIP, SST and PV) together with optogenetics to identify key interactions and a data-driven circuit model to estimate changes in synaptic weights. The model demonstrates that long-range inputs to VIPs that increase visual gain in the locomoting state also govern the time-course of adaptation over the behavioural time-scales of seconds. These inputs do not act uniformly across the PC population but preferentially increase the gain of neurons that sensitize to a high-contrast

stimulus. Contrary to the prevailing model of gain control through the VIP->SST->PC pathway we find that visual responses in SSTs are not inhibited by locomotion but instead weakly enhanced. The model reconciles these observations through a neuromodulatory decrease in synaptic outputs across PCs and interneurons. Locomotion preferentially increases the gain of PCs that undergo the sensitizing form of adaptation because these receive a stronger SST connection than depressor PCs rendering them more sensitive to the weakening of SST synapses. These results provide an integrated view of the circuit mechanisms that adjust visual processing in V1 when an animal switches between resting and active states.

## Results

### Differential effects of locomotion on the fast and slow phases of adaptation

To understand how changes in brain state interact with adaptation in V1 we used two-photon calcium imaging to measure the activity of excitatory and inhibitory neurons in layer 2/3 during periods of rest and locomotion (Fig 1A, see Methods). The GCaMP6f signal in PCs responding to a high contrast stimulus (20º drifting grating at 1 Hz, 10 s duration) are shown in Fig. 1B. Locomotion increased the response averaged across all PCs by a factor of 2.2 ± 0.9. The dynamics of these responses varied widely between individual neurons; while some PCs responded with high initial gain and then depressed, others responded with low initial gain and then sensitized. This heterogeneity is illustrated by the raster plot in Fig. 1B which shows 522 neurons ordered by the time of peak activity: depression (early peak) and sensitization (late peak) were similarly represented in the two behavioural states (Fig 1B, top).

The increase in gain during locomotion was manifested in two ways; a 6-fold increase in the number of PCs generating a significant response (Supplementary Table 1) and an increase in the average amplitude of these responses measured as the integral during the 10 s stimulus (Fig. 1B). To investigate how these changes in gain affected PCs undergoing different forms of adaptation we split the population into three groups of equal size based on the distribution of a metric called the adaptive index (AI; Methods). These groups were sensitizing (AI less than zero), intermediate and depressing (AI more than zero; Fig. 1C). The AI, when computed separately for rest and locomotion and averaged across the whole PC population, was similar during locomotion (-0.006 ± 0.3; mean ± sem) and rest (0.001 ± 0.9; Fig. 1C) but the amplitude of the visual response increased by a factor of 4.5 ± 0.7 in sensitizing PCs, 2.5 ± 0.3 in intermediate group and 2.2 ± 0.2 in depressors. Locomotion therefore increased the gain of sensitizing PCs about twice as strongly as depressors (Fig. 1D-G).

Locomotion was associated with a second notable change in the dynamics of the PC population – a narrower distribution of adaptive effects (Fig. 1C). Cells that depressed at rest showed a shift towards sensitization, while cells that sensitized showed a shift towards depression (Supplementary Figure 1). Although this convergence may partly reflect differences in variability between states, the more uniform dynamics of adaptation parallels the increased temporal correlation observed across the PC population in behavioural states characterised by locomotion[24].

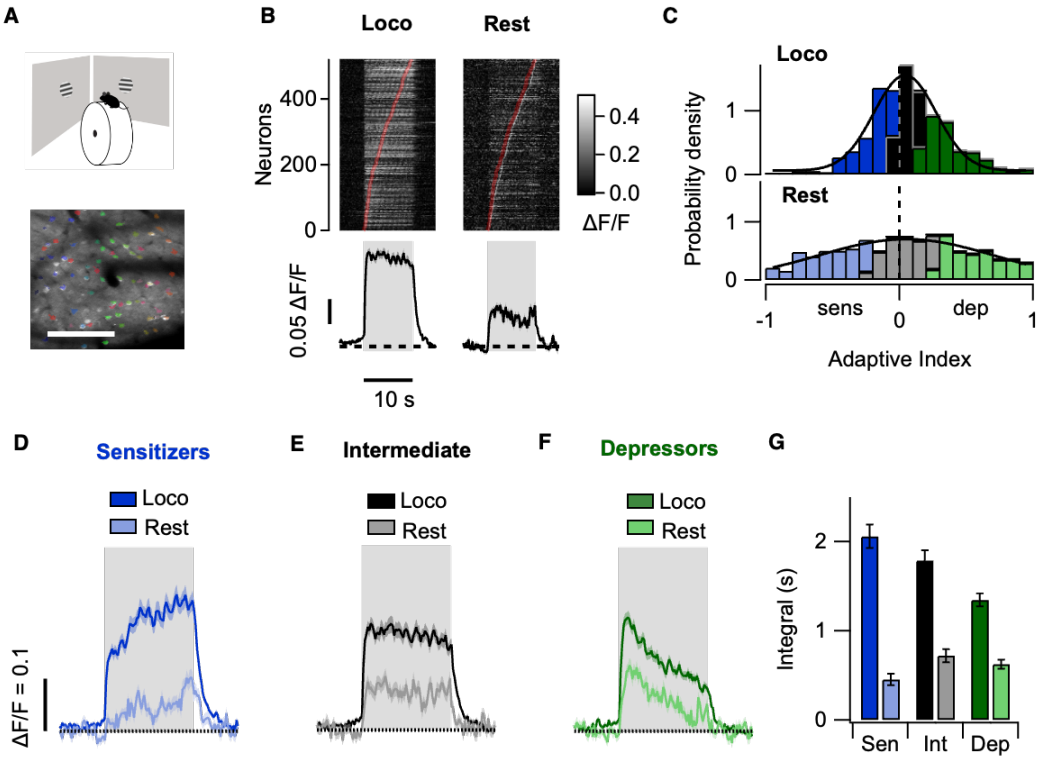


**Figure 1. Slow adaptation in pyramidal cells during rest and locomotion.**

**A.** Top: Mice running on a treadmill were shown a visual stimulus (drifting grating, 20º in size) for 10 seconds. Bottom: example field of view (FOV) showing PCs in V1 expressing GCaMP6f (grey) and corresponding regions-of-interest (ROIs) for individual neurons (rainbow). Scale bar represents 200 µm and stimulus lasts 10 s. **B.** Top: raster plots showing average calcium responses from individual PCs that were responsive to the stimulus during locomotion and rest (Same cells recordings between rest and locomotion, n = 522 neurons, from 9 mice, cells nested within animals). Responses are averaged over 10 stimulus trials then sorted by time of maximum amplitude in rest and locomotion independently. Bottom: average calcium response of all PCs to the visual stimulus during locomotion (left) and rest (right). **C.** Distributions of adaptive indices (AIs) in the PC population during locomotion (top) and rest (bottom) in sensitizers (blue), intermediate cells (grey) and depressors (green). Both distributions can be described by Gaussians with similar $x_0$ and different width (Rest, $x_0$ =0.001±0.9, width = 0.93±0.4; Loco, $x_0$ = -0.006±0.3, width = 0.33±0.02). **D, E, F.** Splitting the distribution of PCs according to their AI reveals that the tertile with lower AI showed slow sensitization, the tertile with intermediate values showed little adaptation, and the tertile with higher AI showed slow depression. **G.** Differences in gain of sensitizers (blue), intermediate cells (grey) and depressors (green) measured as the integral during the stimulus show that locomotion caused a stronger gain increase in sensitizers than in depressors ($p < 0.001$, Linear Mixed Model).

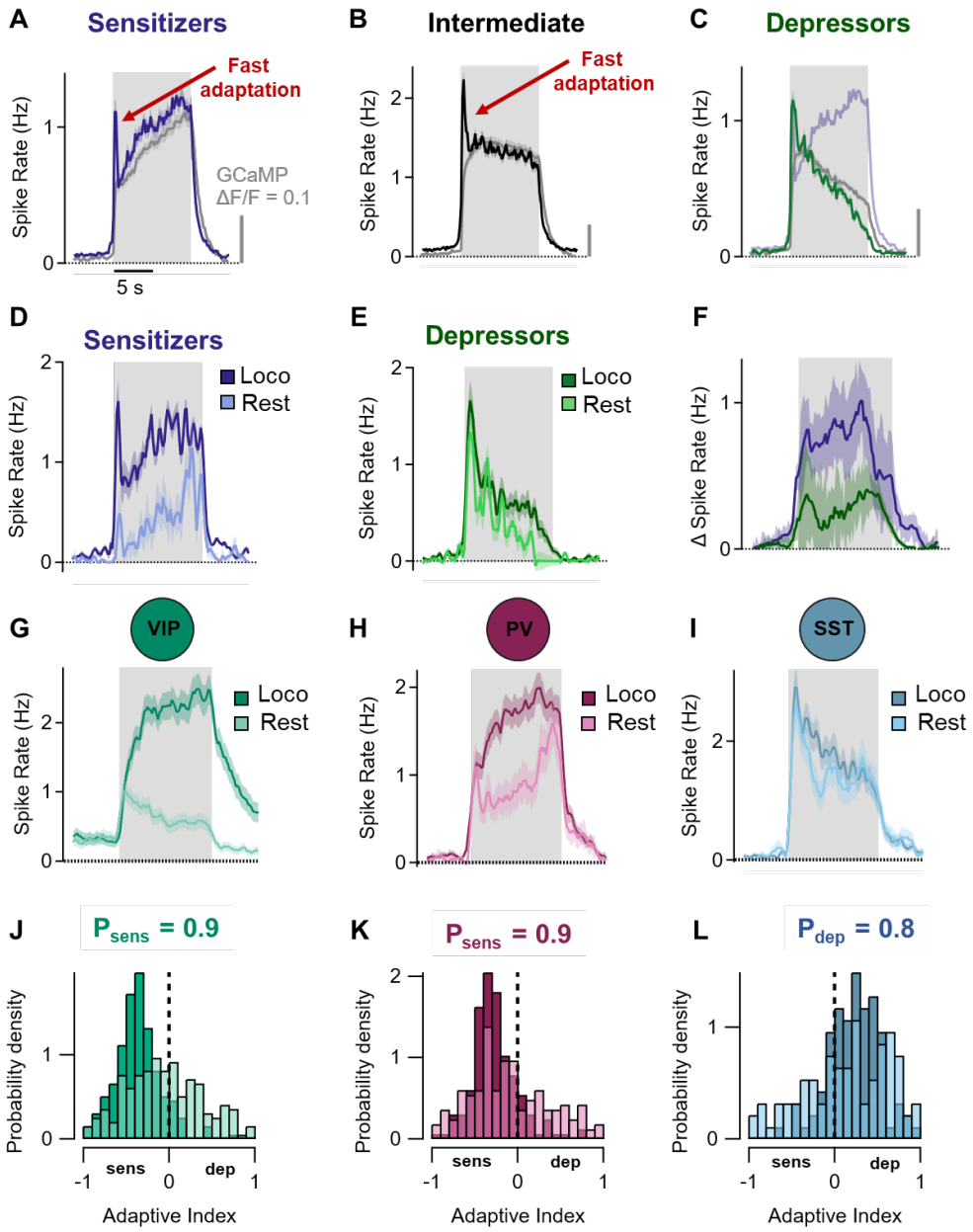


**Figure 2. Differential effects of locomotion on fast and slow components of adaptation in PCs and interneurons.** **A.** Estimated spike rate averaged across all sensitizing PCs measured during locomotion (Data from all neurons responsive to the stimulus during locomotion including non-responsive cells during rest, n = 479 neurons from 14 mice). The GCaMP signal averaged across the same set of neurons is shown in grey. The fast depressing component of adaptation is highlighted by the red arrow. Stimulus duration 10 s. **B.** As A, but for the second (pre-dominantly non-adapting) tertile of PCs. **C.** As A, but for the depressing tertile. The trace from A is superimposed (light blue) showing the almost identical initial amplitude of the response in sensitizing and depressing PCs. **D.** Comparison of average spiking response at rest and during locomotion in the sensitizing tertile of PCs in which paired measurements were made (158 neurons in 9 mice). The relative change in the response during locomotion was 4.7 ± 1. **E.** Comparison of average spiking response at rest and during locomotion in the depressing tertile of PCs. The relative change in the response during locomotion was 1.4 ± 0.3 which was significantly smaller than the sensitizing tertile (T-test, $p < 0.001$). **F.** The time-varying difference in spike rate of sensitizing and depressing PCs. **G.** Average response of VIPs to the visual stimulus during locomotion and rest. The gain during locomotion increased by factor of 5.1 ± 1.0, measured from the integral of the responses. **H.** Average response of PVs to the visual stimulus during locomotion and rest. The gain

during locomotion increased by factor of 1.7 ± 0.2. **I.** Average response of SSTs to the visual stimulus during locomotion and rest. SSTs showed a much smaller, nonsignificant, gain change 1.2 ± 0.2, p = 0.28. **J.** Distribution of adaptive indices in VIP interneurons (n = 122 neurons in 2 mice). Note that AI was measured from GCaMP signals, as for PCs in Fig. 1. VIPs were predominantly sensitizing. $P_{sens}$ = 0.56 at rest and 0.90 during locomotion. **K.** Distribution of adaptive indices in PVs (n = 97 neurons in 3 mice). PVs were predominantly sensitizing. $P_{sens}$ = 0.64 at rest and 0.86 during locomotion. **L.** Distribution of adaptive indices in SSTs (n = 82 neurons in 4 mice). SSTs were predominantly depressing at rest and during locomotion. $P_{sens}$ = 0.37 at rest and 0.21 during locomotion. Results from D to L are from cell-paired recordings in the two states.

The immediate spiking response to a high-contrast stimulus is dominated by depressing adaptation[7,8] but the raw signal from calcium reporter proteins such as GCaMP does not easily distinguish this phase because of the gradual accumulation of calcium in the neuron. Several algorithms for estimating spike rates from calcium signals are now in use[25-27] and we applied MLspike because it is based on a biological model of GCaMP activation and calcium dynamics that has been shown to perform better than others[28] (Fig. 2-A-C). The first component of the spiking response was followed by fast depressing adaptation, as expected from electrophysiology[7,8,29] (red arrows In Fig. 2A-B). During locomotion, the initial peak amplitude was not significantly different in PCs that depressed (1.15 ± 0.08 Hz) or sensitized (1.11 ± 0.08 Hz), indicating similar strength of the feedforward input across the PC population (Fig. 2C).

Comparing activity at rest and while running revealed a powerful effect on both first and second phases of the response but this varied across the PC population. In the sensitizing tertile the initial peak driven by feedforward input underwent a relative increase of 2.1 ± 0.7 and the response integrated over the whole stimulus period a relative increase of 4.7 ± 1 (Fig. 2D). But in the depressing tertile, locomotion did not significantly change the initial fast response while the integrated response only increased by a factor of 1.4 ± 0.3 (Fig. 2E). Changes in internal state associated with locomotion do not, therefore, act uniformly across the PC population but preferentially increase the gain of neurons that undergo the sensitizing form of adaptation (Fig. 2F).

**A data-driven model of contrast adaptation and the effects of locomotion**

To understand how an active behavioural state differentially alters gain across PCs we constructed a population model of signal flow based on neuronal input-output functions expressed as firing rates[30-32] (see Methods). The model took into account three aspects of circuits in layer 2/3: *i)* the measured response dynamics of PCs and the three major types of interneurons (Fig. 2G-L); *ii)* the dynamics of signals that arrive from other brain regions (Fig. 3A), and *iii)* the known connectivity patterns of neurons within this layer (Fig. 3B). Code and example data sets are available at https://github.com/lagnadoLab/CortexModel.

***i) The dynamics of neurons in layer 2/3***

A key determinant of the magnitude and direction of slow adaptive changes in a PC is the local inhibitory microcircuit in which it is embedded: PCs in which direct SST inputs dominate over PV inputs tend to sensitize while those in which PV inputs dominate depress[9]. We therefore also experimentally measured the effects of locomotion on gain and adaptation in the three major interneuron types to use their response dynamics in the model (Fig. 2G-L). VIPs underwent the strongest modulation: the density of responsive neurons changed by a factor of 3 (Supplementary Table 1), and the integrated amplitude of these responses by a factor of 5.1 ± 1.0 (Fig. 2G). Simultaneously, locomotion caused the ratio of sensitizing (AI <0) to depressing (AI > 0) VIPs to increase from 1.3 at rest to 9 (Fig. 2J). PVs were more weakly modulated, with integrated responses changing by a factor of 1.7 ± 0.2 while the ratio of sensitizers to depressors also increased from 1.8 to 6.1 (Fig. 2H and K). In contrast, locomotion did not significantly alter the number of responsive SST neurons or the amplitude of their responses (gain factor of 1.2 ± 0.2; p = 0.28; Fig. 2I and L). This observation was surprising given that VIPs powerfully inhibit SSTs and locomotion activates a VIP->SST->PC disinhibitory pathway often highlighted as an important contributor to gain control[11,33,34]. However, the influence of this pathway is known to vary, consistent with reports that SST response to locomotion depend strongly on the visual stimulus[3,12]. A major aim of the model, therefore, was to take a more integrated view of gain control that considered multiple interacting pathways within layer 2/3.

The distribution of response dynamics in interneurons was more homogeneous than in PCs. The probabilities of a PC being sensitizing (AI <0, $P_{sens}$) or depressing (AI > 0, $P_{dep}$) were both ~0.5 (Fig. 1C), but during locomotion sensitization dominated in VIPs and PVs ($P_{sens}$ = 0.9) while depression dominated in SSTs ($P_{dep}$ = 0.8; Fig. 2J-L). These more consistent, cell-type-specific dynamics allowed us to represent each interneuron class by its characteristic average response (Fig. 2G-I), which we used as empirical input to a population mean-field model. Mean-field models have been widely used to describe the average behaviour of large populations of interacting neurons without simulating each neuron individually[30,35,36]. The network was represented by a system of four first order ordinary differential equations[30]:

$$\tau_i \frac{dr_i}{dt} = -r_i + f\left(\sum_j w_{ji} r_j + w_{in} In + b_i\right) \qquad (1)$$

where $i, j$ are iterating through the four neuronal populations (PC, VIP, PV and SST), $j$ is a presynaptic population and $i$ postsynaptic, $r$ is a firing rate and $\tau_i$ is the time-constant for that population. $f(x)$ is a neuronal input-output function and here we used a rectified power law[32]. The terms $w_{in} In$ express the connection weights and amplitude of external inputs, and $b_i$ the baseline activity of postsynaptic cell i. The connection weight between populations *j* and *i*, $w_{ji}$, is

217 simply the product of the total number of synaptic connections, $C_{ji}$, and the average strength of
218 an individual synapse between neuron type j and i, $s_{ji}$:
219
220 $$w_{ji} = C_{ji} s_{ji} \quad (2)$$
221
222 To compare the model to experiments, it was important to consider that not all presynaptic
223 neurons are activated by the stimulus and, even if they are, they do not all activate the
224 postsynaptic population because the connection probability ($p_{ji}$) is usually less than one. If, for
225 instance, electrodes are placed on a PC and a nearby PV interneuron the probability of them
226 being connected is only ~0.37 at distances less than ~150 μm while the average probability of an
227 SST interneuron is even lower at ~0.27[37-39]. These factors can be taken into account by
228 expanding relation 2 as
229
230 $$s_{ji} = {}^{w_{ji}}/_{N_j p_{ji}} \quad (3)$$
231
232 where $N_j$ is the number of *responsive* presynaptic cells, defined as described in Methods. Below
233 we infer changes in individual synaptic weights ($s_{ji}$) associated with a transition into the active
234 state by comparing experimentally measured changes in $N_j$ (Supplementary Table 1) to changes
235 in connection weights ($w_{ji}$) estimated by fitting the model.
236
237 ***ii) The dynamics of signals entering layer 2/3.***
238 Excitatory signals entering layer 2/3 are of three main types[40,41]: feedforward (FF) drive originating
239 from the lateral geniculate nucleus (LGN) and transmitted via layer 4, feedback from higher order
240 cortices (FB)[42,43] and modulated inputs (SS), such as those gated by cholinergic signals from the
241 basal nuclei[11]. Electrophysiology has shown that FF inputs to layer 2/3 are dominated by fast
242 depressing adaptation occurring within a few hundred milliseconds and the fast phase of
243 adaptation in PCs fell within this range[7,8] (Fig. 2A-B). Calcium imaging *in vivo* has shown that
244 drifting gratings lasting seconds can also generate a slower sensitizing component in FF inputs
245 that enter layer 2/3 from layer 4[22,44]. The FF input was therefore modelled with both these
246 components, as shown in Fig. 3A.
247 The second type of input to V1 is feedback from higher visual areas[45-47] and SST
248 interneurons are one of their targets[46,48,49]. We have limited understanding of the dynamics of the
249 FB signal over the time-scale of our stimulus, so, for simplicity, it was modelled as a step
250 beginning at a delay of 380 ms after stimulus onset (Fig. 3A).

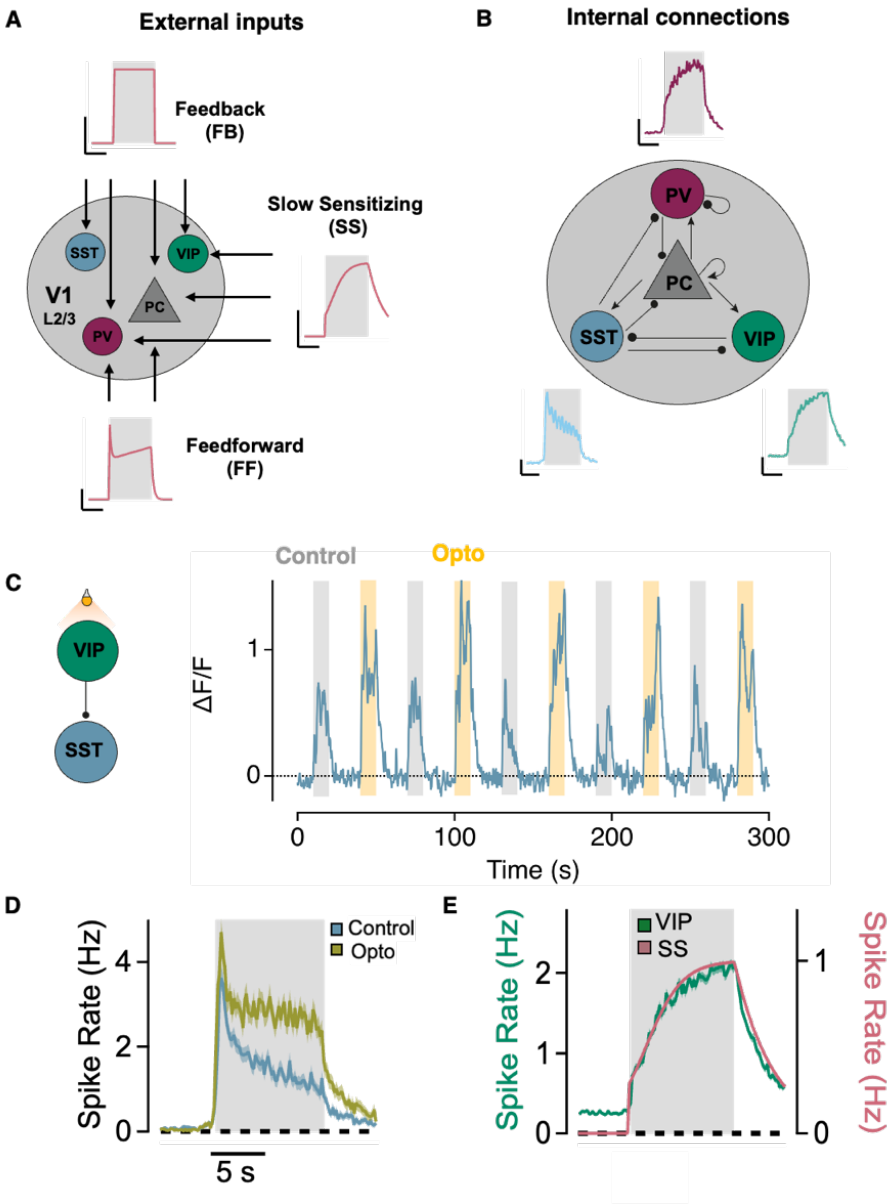


**Figure 3. A model of signal flow in layer 2/3.**

**A.** Schematic showing the targets of three external inputs into layer 2/3 of V1. Feedforward excitation targets PVs and PCs; feedback input targets all populations [50,51] and the slower sensitizing input enters through VIPs as well as directly activating PCs and PVs[52]. (Vertical bar: 0.5 Hz, horizontal bar: 5 s) **B.** Schematic showing the main excitatory (arrow tip) and inhibitory (round tip) connections between cell types within L2/3 of V1. PCs form excitatory connections with all other neuron types including themselves. PVs mainly target PCs and other PVs while SSTs inhibit all other cell types but avoid inhibiting each other. VIPs almost exclusively inhibit SST interneurons. (Vertical bar: 0.05 ΔF/F, horizontal bar: 5 s). **C.** Left: schematic showing the experimental paradigm to test if VIPs were a target for a slow sensitizing signal driving adaptation in layer 2/3: VIPs were silenced optogenetically while simultaneously recording activity in SSTs. Right: example response of an SST neuron during stimulus presentation alone and stimulus paired with optogenetic silencing of VIPs. **D.** Average response of SSTs with and without optogenetic silencing of VIPs (n = 83, from 4 mice). Silencing VIPs almost completely blocked slow adaptation. Light grey shade shows the stimulus time (10 s). **E.** The slow sensitizing input to the model (SS) was based on the average response of the VIP population during locomotion and consists of a step and sigmoid function with a time-constant = 1.71 s.

The third type of inputs to layer 2/3 are visually-activated signals that are strongly sensitizing in the locomoting state and drive slow sensitization. The dynamics of this signal were inferred from the visual response of VIPs measured experimentally during locomotion (Fig. 2G). We used these measurements because optogenetic experiments confirmed that activity in VIPs drove adaptation in downstream SST neurons, to which they are known to connect strongly[11,33,34] (Fig. 3C-D). To carry out this test we had to express the inhibitory photoprotein ArchT in VIPs and GCaMP6f in SSTs. Expressing different proteins in two interneuron populations was achieved by crossing a recombinant mouse line expressing Cre (VIP-Cre) with a Flippase expressing line (SST-Flp), then injecting two viral vectors that were Cre and Flippase dependent respectively (see Methods). Suppressing activity in VIPs almost completely abolished the slow component of adaptation in SSTs (Fig. 3D). Visually-driven inputs to VIPs include local recurrent excitation[33] and inputs from higher visual areas[53], and the combined dynamics of the later were modelled on the VIP response (Fig. 3E). This slow sensitizing signal appears quite distinct from inputs from the basal forebrain which provide a binary locomotion state signal but have been found *not* to respond to visual stimuli[54]. Notably, the dynamics of sensitization in VIPs were similar to sensitization in PCs suggesting that this input dominated slow adaptation throughout the network (Supplementary Figure 2).

***iii) Connectivity within layer 2/3***

Cortical connections have been probed using a number of approaches, including viral tracing[55], electrophysiology[33,37,39] and optogenetics[38], and we only considered connections that have been consistently observed in layer 2/3 and are strong enough to significantly influence the circuit (Fig. 3B). Not all neuron types connect; SST interneurons, for example, do not interact with each other while the very small number of connections from VIPs to PCs were neglected because these are not strong enough to significantly influence the circuit[33,38].

**Using optogenetic manipulations to constrain model solutions and test its predictive ability**

The model was fit to average populational responses of PCs and interneurons by adjusting the weights $w_{ji}$ of external and internal connections in layer 2/3 (see Methods). Given the large parameter space spanned by the model, many solutions were of similar quality. Rather than identifying a single optimal solution, our fitting procedure revealed a region of parameter space that yielded good fits.

First, we generated 100,000 sets of evenly distributed initial parameters using Sobol sampling[22,56,57]. Of these, only 37 produced “good” solutions with chi-square < 10 in the locomotion condition, defining the approximate boundaries of the viable region. Next, this

302 parameter subspace was explored further by local optimization using 20,000 Sobol initial
303 conditions for each synaptic weight. This produced ~9000 good solutions in the locomotion
304 condition with similar average and standard deviation to the initial 37. We then applied a third
305 stage involving a series of experiments in which interneuron activity was altered optogenetically,
306 which constrained the number of good solutions (to ~900) and the viable region of parameter
307 space (Fig. 4). This third stage could not be usefully applied to data at rest because there were
308 not enough recording episodes across all four optogenetic conditions and responses were smaller
309 and more variable than during locomotion[24]. We therefore limited the number of solutions by
310 using a lower chi-square value of 3. The average parameter values after reducing the number of
311 good solutions through all the steps are used to analyze the predictions of the model in Figs. 5
312 and 6.

313 The first optogenetic manipulation was to over-activate SSTs by expressing the excitatory
314 photoprotein ChrimsonR using a Cre-dependent viral vector. Simultaneously, responses were
315 recorded in PCs using GCaMP6f under the CaMKII promoter. The intensity of the photo-
316 activating light was adjusted to increase the activity of SST interneurons by an average factor of
317 ~2 in locomoting animals, as estimated in a separate series of experiments[9]. Fig. 4A (top) shows
318 how the average PC response in the locomotion state was reduced compared to interleaved
319 control trials.

320 Scaling the average SST activity within the model by a factor of 1.7 while leaving all other
321 parameters constant provided an accurate description of the change in average PC activity in
322 only 74% of the original ~9000 solutions (Fig. 4C). In other words, although a broad region of
323 parameter space could reproduce the control data, introducing this optogenetic manipulation
324 eliminated roughly one-quarter of the solutions, thereby narrowing the admissible parameter
325 space.

326 After this first filtering step, we sequentially reduced the number of good solutions by
327 constraining to results of SST silencing, PV activation and PV silencing, in this order. We found
328 that while SST silencing and PV activation reduced the number of solutions to 25% and 11% of
329 the original 9000, adding the last filter, PV silencing, had little further effect (Fig. 4C). Furthermore,
330 connection weights remained identical when applying the first three optogenetic constraints
331 compared to applying the fourth (Fig. 4D). PV silencing therefore served as a validation step: it
332 confirmed the region of parameter space defined by the three previous filters instead of further
333 refining it.

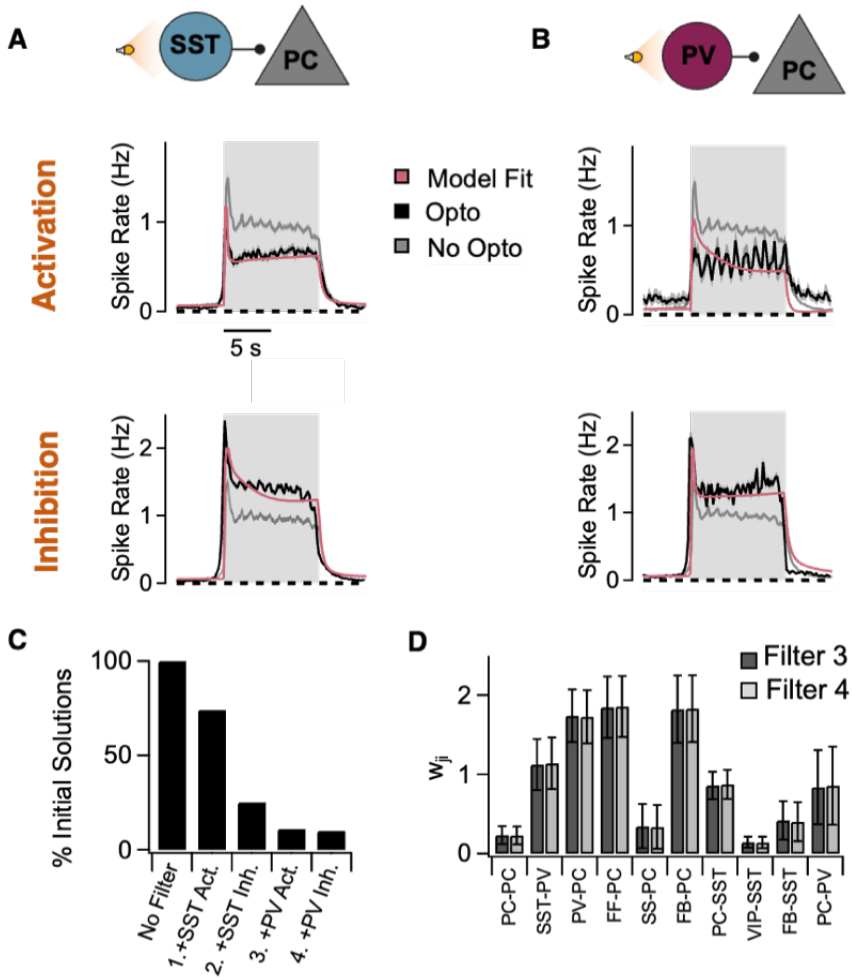


**Fig. 4. Testing the model using optogenetics**

**A.** Top: Average PC response with and without optogenetic activation of SSTs. Separate experiments indicated that this intensity of photoactivating light increased SST activity by a factor of ~1.7[9]. The red trace shows the model prediction when SST activity within the model was increased by the same factor. Activation of SSTs decreased PC gain and increased sensitization (top, RMSE = 0.27). The grey control trace (No Opto) is averaged over all four optogenetic conditions in A and B. Bottom: Average PC response with and without optogenetic inhibition of SSTs. Separate experiments indicated that this intensity of photoactivating light decreased SST activity by a factor of ~1.9[9]. The red trace shows the model prediction when SST activity within the model was decreased by the same factor. Silencing of SSTs resulted in an increase in gain and a shift to more depressing dynamics (bottom, RMSE = 0.31). **B.** Same as in C but when PVs were optogenetically activated (top, by a factor of ~2.5) or silenced (bottom, by a factor ~2.0) during stimulus presentations. Activation of PVs decreased the gain of PCs (top, RMSE = 0.32). Silencing of PVs resulted in an increase in gain and shift to more sensitizing dynamics (bottom, RMSE = 0.28). **C**. Proportion of the initial "good" solutions to the model (chi-square < 10) that also provided good solutions incorporating the results of the optogenetic manipulations in A and B. Filtering of solutions on the basis of adding optogenetic conditions was carried out in series in the order 1-4. Applying filter 4 (PV inhibition) had little further effect on the number of good solutions i.e almost all good solutions incorporating manipulations 1-3 also predicted the effects of PV inhibition. **D**. Comparison of connection weights (mean ± SD) of all good solutions after applying optogenetic filters 1-3 and 1-4. All weights remain similar after the fourth filter and it is these averages that are presented in Figs. 5 and 6.

**Locomotion increases PC gain but weakens their local synaptic output**

Behavioural modulation of connection weights *within* layer 2/3 have been very hard to quantify experimentally, making it unclear how far changes in internal state adjust cortical processing through changes in neuronal activity as opposed to modulation of synaptic weights[14,16]. We used the model constrained by the four optogenetic manipulations to infer changes in synaptic weights. First, we investigated the action of locomotion averaged across the whole PC population (Fig. 5) and then explored why the subset of PCs that sensitize is modulated more strongly than those that depress (Fig. 6).

All the model solutions that allowed a good fit to the average visual responses in the four cell types closely followed both the fast and slow phases of adaptation at rest and during locomotion, as exemplified by the average solution (Fig. 5A-D, Supplementary Figure 3). Unsupervised clustering analysis identified a single cluster of solutions for locomotion and another for rest, indicating that these parameter sets form a continuum rather than falling into distinct categories. Moreover, examination of the distribution of each parameter revealed that all were unimodal, with no evidence for multiple peaks or clusters (data not shown). This pattern is consistent with gradual transitions within a single family of network configurations and supports the use of the mean as a representative summary. The average connection weights (Equation 2, $w_{ij}$) at rest are shown in the heatmaps in Fig. 5E and the relative changes with locomotion are summarized in Fig. 5F, calculated as:

$$[w_{ij(\mathrm{loco})} - w_{ij(\mathrm{rest})}] \,/\, w_{ij(\mathrm{rest})} \qquad (4)$$

Where free parameters predicted by the model could be compared with published experiment, there were several points of agreement. For instance, the relative strength of direct local connections to PCs were quantitatively similar to those measured using electrophysiology[37,38]. There were, however, differences with other attempts to infer connection weights. Using our nomenclature, a recent modelling study[23] inferred a weight order in V1 at rest of $w_{PC_PV} < w_{PC_PC} < w_{PV_PV} < w_{PV_PC}$, while our results infer $w_{PC_PC} < w_{PC_PV} < w_{PV_PV} < w_{PV_PC}$ (Fig. 5E). This difference may reflect our models incorporation of long-range modulatory inputs, which also allowed it to predict other experimental observations, including a locomotion-dependent amplification of the slowly modulated input to VIPs[11] and PCs[52] and enhancement of feedforward drive to PCs[58,59]. The incorporation of long-range modulatory inputs into the model were essential to accurately estimating connection weights within layer 2/3 because removing these inputs did not yield any solutions following the same quality criteria (Supplementary Fig. 4, see Methods).

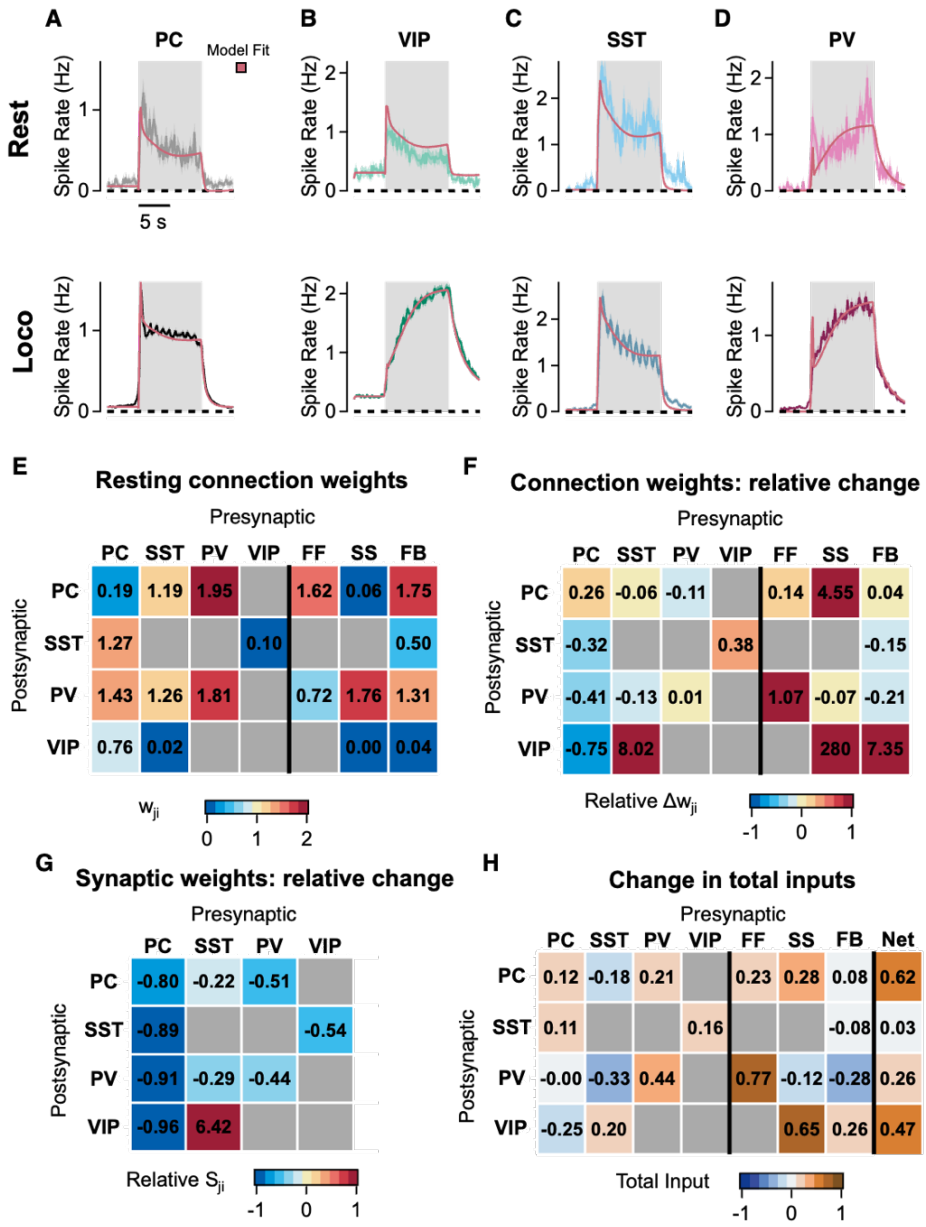


**Figure 5. Locomotion modulates both electrical activity and the strength of synaptic connections.** **A-D.** Top: Average firing rates of PCs (A, black), VIPs (B, green), SSTs (C, blue) and PVs (D, dark red) during stimulus presentation at rest and their corresponding fits from the average of solutions calculated by the model (light red, RMSE = 0.19). Note that these traces show the average activity of only partially paired recordings, where only a subset of cells are matched between rest and locomotion (Rest n=158 from 9 mice, Locomotion n = 1437 neurons, from 14 mice). Bottom: average activity during locomotion in the same neuronal populations (RMSE = 0.11). **E.** Average resting connection weights from all solutions estimated by fitting the model to the activity of responsive neurons (Equation 2). **F.** The relative change in connection weights caused by locomotion (Equation 4). **G.** Relative change in synaptic weights based on estimated changes in connection weights **(F)** and measured changes in number of responsive cells (Supplementary Table 1; equation 3). Note that all excitatory and inhibitory synapses weaken except for synapses from SST to VIP which strengthen. **H.** The change in the total synaptic input activated by the stimulus, calculated from the average activity (Supplementary Table 2) and the change in connection weight in F (equation 5). The last column is the net change taking into account the polarity of the synapse.

The model indicates that locomotion increases the gain of PCs through a broad combination of circuit effects but of particular importance is a 25-50% reduction in the strength of inhibitory synapses made by SSTs and PVs (Equation 3, $s_{ij}$; Fig. 5G). Strikingly, the model also predicts that the *total* weight of connections from PCs to all types of interneurons is decreased by one to three quarters following locomotion (Fig. 5F). The total synaptic input that neuron i receives from j, $I_{ji}$, is proportional to the activity of j and can be expressed as:

$$I_{ji} = w_{ji} r_j \tag{5}$$

Taking into account the 5-fold *increase* in the number of responsive PCs during locomotion (Supplementary Table 1) this leads to an estimated 90% decrease in synaptic strength across all PC targets (Fig. 5G). The model indicates that the large increase in PC and PV activity in the locomoting state is associate with a wide-spread decrease in the strength of their local synapses. This mechanism would allow large changes in the gain of signals *leaving* V1 for higher visual areas but without overexcitation of PC targets *within* the local circuit. The possible cholinergic mechanisms underlying these changes are considered in the Discussion.

In contrast to the rest of the local network, the average SST->VIP connection weight *increased*, by a factor of ~8 (Fig. 5F). The number of responsive SSTs neurons increased by only 22% (Supplementary Table 1) indicating that the major cause was a *strengthening* of SST synapses (Fig. 5G). This differential pattern on excitatory synapses of PCs (suppression) and SSTs contacting VIPs (enhancement) could be consistent with known variations in the distribution of different muscarinic acetylcholine receptors (see Discussion).

Switching to the active behavioural state also increased the strength of specific inputs to layer 2/3, most obviously the FF connections to PVs and the SS and FB connections to VIPs (Fig. 5F). VIPs were the most striking target, explaining their dramatic increase in gain (Fig. 2G).

Another way to summarize the effects of locomotion is to consider the change in the *total* synaptic input (both excitatory and inhibitory) as PCs respond to the visual stimulus (Supplementary Table 2; equation 5; Fig. 5H). The last column in Fig. 5H shows this change, taking into account the input received from all connected populations averaged over the stimulus presentation. The net excitatory input driving the visual response is more pronounced in PCs and VIPs compared to PV and SST interneurons, consistent with the locomotion-associated changes in gain shown in Fig. 2. Notably, the model predicted almost zero net change in total input to SSTs, consistent with the negligible change in SST activity observed experimentally (Fig. 2I) but inconsistent with the simple VIP->SST->PC disinhibitory model. The overarching picture is that locomotion adjusts the gain of visual responses by modulating both excitatory signals entering layer 2/3 and the strength of local synaptic connections, expanding what has been observed in a previous study[12].

441 **Differential modulation of SST inputs onto sensitizing and depressing PCs**

442 Why do some PCs sensitize while others depress? Optogenetic manipulations of interneurons
443 indicate that the direction and amplitude of slow adaptation reflect the balance between PV and
444 SST inputs[9]. PVs sensitize (Fig. 2H), so PCs in which these inputs dominate tend to depress,
445 while SSTs depress (Fig. 2I), causing PCs in which these inputs dominate to sensitize. To make
446 these ideas quantitative, we fit the model separately to the sensitizing, intermediate and
447 depressing PC subpopulations (Fig. 6A-C). At rest, all the external connections to PCs had similar
448 weights irrespective of adaptive properties; the stand-out differences were in the local inhibitory
449 connections (Fig. 6D). In qualitative agreement with the "balance model", the direction of
450 adaptation of a PC was dependent on the ratio of the PV and SST inputs, which increased
451 progressively between the sensitizing, intermediate and depressing populations in both rest (0.9,
452 1.8 and 2.7, respectively; Fig. 6D) and locomotion (1.3, 1.7 and 2.7, respectively, Fig. 6E). We
453 tested this prediction of the model by comparing the effect of optogenetic manipulations of SST
454 and PV interneurons in the locomotion condition, confirming that sensitizers are more influenced
455 by SSTs while depressors are dominated by PVs (Fig. 6F). This balance also influences the
456 release from inhibition that different PCs undergo during locomotion, with sensitizers receiving
457 less inhibition than depressors from SST interneurons, while the inverse pattern is observed for
458 PV connections (Fig. 6G).

459 In principle, the differences in connectivity between sensitizing and depressing PCs could
460 reflect synaptic strength. We found, however, only slight differences in the synaptic weight of all
461 cell types connecting to PCs (Fig. 6H) and similar net total input between depressors and
462 sensitizers (Fig. 6I). Again, the key difference was the SST:PV input ratio: sensitizers
463 experienced a pronounced decrease in total SST inputs and increase in PV input (Fig. 6I).
464 Notably, the increase in PC gain associated with locomotion did *not* correlate with changes in
465 total inhibitory input (Fig. 6I), consistent with evidence that inhibition acts divisively rather than
466 subtractively[60,61,62] (see Discussion). Overall, these results support the view that the enhanced
467 gain observed in sensitizers is the result of their heightened exposure to a reduction in SST
468 inhibition during locomotion.

469

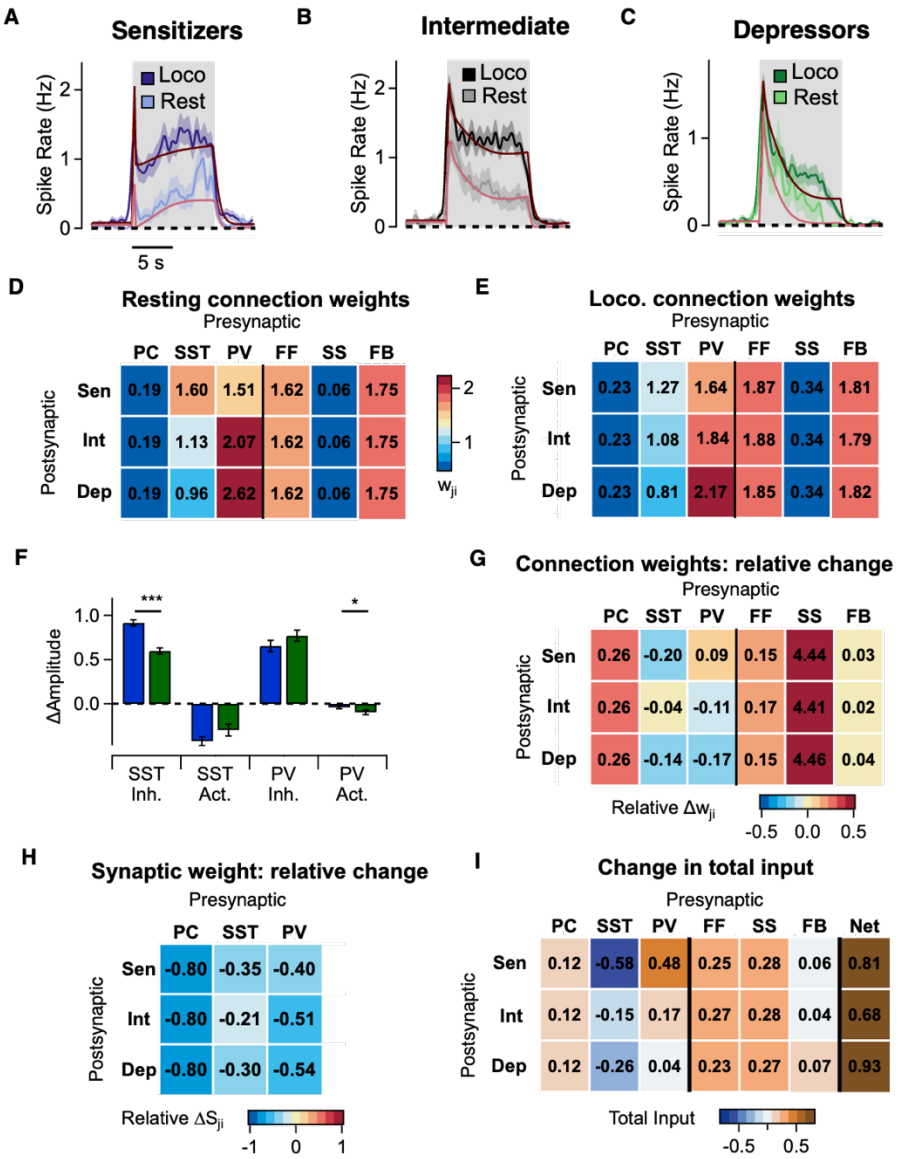


**Figure 6. Differences in PV:SST input ratio determine the direction of PC adaptation and the change in gain associated with locomotion.** **A.** Activity of PCs from the tertile with lower AIs (sensitizers) at rest and during locomotion together with fits from the average of all good solutions calculated by the model (rest, RMSE = 0.22; loco, RMSE = 0.17). These are paired measurements from 158 neurons in 9 mice. During locomotion 7.5 ±1.2 more spikes were fired during the stimulus. **B-C.** As A, but for the intermediate and depressing tertiles, RMSEs were similar to sensitizers. During locomotion the stimulus generated 6.3 ± 0.9 more spikes in the intermediate group and 2.8 ± 0.4 in depressors. **D-E.** Heatmaps of the synaptic weights for each PC tertile at rest (D) and locomotion (E); sensitizers (Sen), intermediate (Int) and depressing (Dep). **F.** Amplitude change induced by optogenetic manipulation of SSTs and PVs in sensitizer (blue) and depressing (green) PCs. Note that sensitizers are preferentially modulated by SSTs and depressors by PVs as predicted by the model. (Inh: silencing with ArchT, Act: activation with ChrimsonR). **G.** Relative change in connection weights caused by locomotion for each subpopulation of PCs (calculated as equation 4). The key difference is the relative strength of PV and SST inputs. **H.** Relative change in synaptic weights caused by locomotion for each subpopulation of PCs. **I.** Change in total input during presentation of the stimulus received by each subpopulation of PCs. Sensitizers receive less SST inhibition than the intermediate and sensitizing tertiles. The last column shows the *net* change in total input, taking into account the polarity of the synapse.

## Discussion

Adaptation is a fundamental aspect of sensory processing across cortical areas but it has not been clear how it is adjusted by changes in behavioural state that modulate these circuits. Here we have demonstrated that an active state acts on V1 to preferentially amplify responses in PCs that exhibit sensitizing adaptation over behavioural time-scales, with minimal effects on depressing PCs (Figs. 1 and 2). A data-driven network model indicates that locomotion modulates both the external inputs arriving to V1 and local synaptic connections. The differential modulation of the PC population reflects variations in their local inhibitory circuits: sensitizing PCs receive proportionally stronger SST input relative to PV input making them more susceptible to the locomotion-driven decrease in SST inhibitory strength (Fig. 6). More generally, these results build from the simple model of gain control through the VIP→SST→PC disinhibition pathway [11,63] by also considering the broader neuromodulatory actions of the cholinergic input to V1. The results, summarized in Fig. 7, indicate that locomotion increases the gain of PCs through a combination of circuit effects, including an increase in external inputs and a decrease in local inhibition (Figs. 5 and 6). We have not so far been able to identify other functions that correspond with sensitizing and depressing PCs: the initial gain of the visual response (Fig. 2C), receptive field location[9] and orientation tuning[9] are not significantly different between these groups.

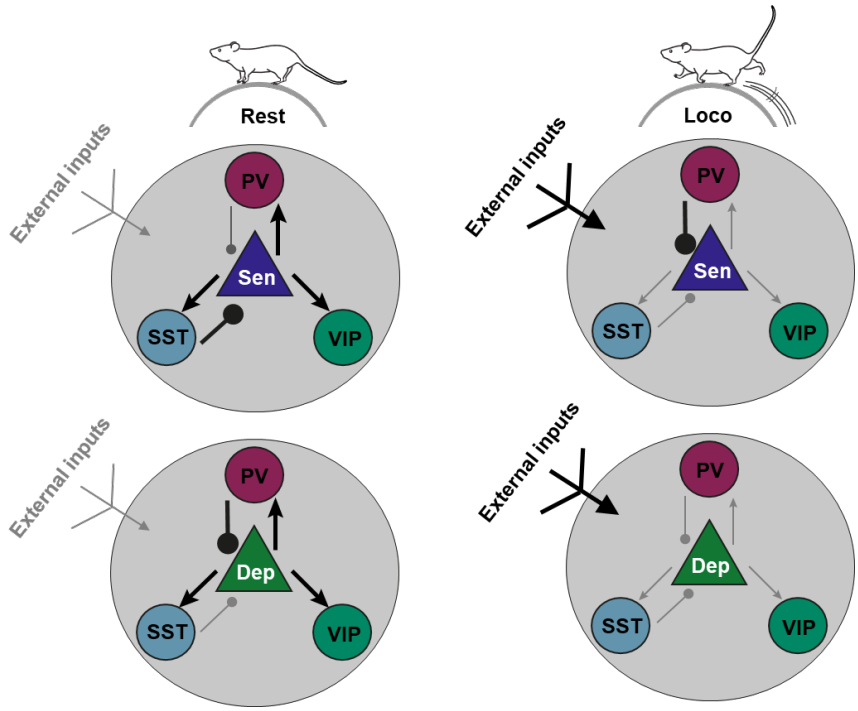


**Figure 7. Summary of effect of locomotion in V1.** From rest (left) to locomotion (right) the connections from external inputs increase while the strength of PC connections to other targets is reduced. Sensitizers (top) receive stronger SST inhibition, being more sensitive to their reduction during locomotion, while depressors (bottom) receive stronger PV inhibition.

510 **Gating of the feedforward signal**

511 The increase in gain during locomotion was profound: the number of PCs responding to the
512 stimulus increased by a factor of six (Supplementary Table 1) and the average amplitude of those
513 responses by a factor of 2-3 (Figs. 1 and 2). About 70–80% of PCs in layer 2/3 send axon
514 collaterals to higher visual areas[64,65] so these combined effects will strongly amplify the
515 feedforward visual signal, at least to the drifting grating stimulus used here. The local recurrent
516 signals are, however, strongly damped by a wide-spread decrease in the strength of recurrent PC
517 synapses subject to local modulation (Fig. 5). This decoupling of spiking activity and synaptic
518 efficacy suggests a mechanism by which V1 can amplify its output to downstream targets, such
519 as higher visual areas, without generating excessive excitation in the local recurrent network.
520 Such a mechanism could be important for maintaining the stability of computations that rely on
521 balanced excitation and inhibition within V1. We suggest that the suppression of PC output
522 reflects a gating mechanism that allows feedforward communication to be selectively boosted
523 while shielding local circuits from saturation. This prediction could be tested by performing paired
524 electrophysiological recordings of PC→PC connections during state transitions, but direct
525 measurements of changes in synaptic strength in the cortex of behaving mice are currently
526 extremely challenging - most of the available evidence is inferred from circuit-level activity
527 patterns and *in vitro* studies.

528 Acetylcholine release triggered by activity in the basal forebrain and prefrontal cortex acts
529 across large areas through volume transmission[15,66] but different muscarinic receptor types are
530 expressed at specific locations, very often presynaptically, which provides spatiotemporally
531 specific modulation[67]. The reduction in strength of local PC synapses during locomotion inferred
532 from the model is in line with the known actions of acetylcholine on presynaptic M2 receptors,
533 which reduce glutamate release at PC terminals[16-18]. Many cortical areas are subject to
534 modulation through the cholinergic input that they receive [15,66], raising the possibility that signals
535 from the basal forebrain also contribute to the increase in external input predicted by the model
536 (Figure 5F).

537

538 **Locomotion shapes cortical dynamics through multiple pathways**

539 The first effect of locomotion was to enhance a slow sensitizing signal activated by the visual
540 stimulus, the major target of which was VIP interneurons (Fig. 3). The source of this signal is
541 likely the higher visual areas[43] gated by acetylcholine, and optogenetic experiments demonstrate
542 that it determined the dynamics of adaption in SSTs (Fig. 3 and Supplementary Figure 2). The
543 second major effect predicted by the model was an over 90% reduction in the strength of PC
544 synapses across all targets (Fig. 5G), consistent with a range of evidence obtained *in vitro*
545 demonstrating that M2 muscarinic receptors cause presynaptic inhibition[16,17,68]. A similar
546 mechanism likely operates at PV, where release probability is reduced by M2 and M4 receptors[69-

547 [71]. However, the situation is different for SST interneurons. Our modelling shows that VIPs
548 receive weak SST inputs at rest and that these synapses are *potentiated* during locomotion (Fig.
549 5E-G). This is likely to reflect a post-synaptic action of M1 receptors which have been shown to
550 enhance postsynaptic $GABA_A$ currents in visual and somatosensory cortices[71,72]. In contrast, SST
551 inputs to PCs and PVs appeared *weaker* during locomotion.
552 SSTs are a heterogenous class of inhibitory cells that target other cortical neurons in two
553 distinct ways. The most numerous subtype, Martinotti cells, synapse on distal apical dendrites of
554 PCs in layer 1 and show strong depressing adaptation, while Non-Martinotti cells generate more
555 variable responses[48,73,74]. We suggest that SSTs contacting VIP interneurons are predominantly
556 Non-Martinotti cells because they are the only subtype known to be enhanced by acetylcholine
557 through M1 and M3 receptors *in vitro*[75]. It may also be that other neuromodulatory systems
558 contribute to these mixed effects, including noradrenaline, serotonin and dopamine[2,11]. The
559 models might be refined by splitting SSTs into two populations once their responses are
560 measured separately[76], but a more critical next step is to test the predicted changes in synaptic
561 strength. As for PC→PC connections, the best way to test this would be to make paired
562 electrophysiological recordings of identified SST→PC and SST→VIP connections during state
563 transitions.
564 A key insight from our modelling is that the relative strength of PV and SST inputs predicts
565 both the direction of PC adaptation *and* the degree of locomotion-induced gain modulation (Fig.
566 6). Depressing PCs receive stronger PV input, consistent with their rapid and temporally precise
567 inhibition[77]. In contrast, sensitizing PCs receive relatively stronger SST input which slowly
568 depress to drive sensitization[9]. These differences in PV:SST ratio may also contribute to the
569 changes in gain associated with locomotion: because SST→PC inputs decrease substantially
570 during locomotion (Fig. 5), PCs already dominated by SST input exhibit the largest gain
571 enhancement. It is well established that there are substantial variations in the inhibitory input
572 patterns to PCs but it is unclear how far these reflect the development of specific wiring patterns
573 as opposed to the variability that will arise from random connections[37,78,79]. PV and SST
574 interneurons are much sparser than PCs[80] and connect to them with low probabilities[37,39], such
575 that simple random connectivity can give rise to PCs receiving different proportions of PV and
576 SST inhibition – a pattern that at least partially occurs in V1[81].
577
578 **Modulation of SST→PC inputs during changes in brain state**
579 An intriguing prediction of our model is that the number of SST→PC synapses onto sensitizing
580 PCs weaken whereas their PV→PC inputs increase selectively during locomotion (Fig. 6I). As a
581 result of these opposing effects of inhibition, the total net input does not differ substantially from
582 that of depressor PCs. There has been controversy regarding the computational form of SST and
583 PV inhibition onto PCs: under certain experimental conditions SST inhibition has been described

as subtractive and PV divisive[60], while different manipulations show the opposite[61,62]. Although in our model we initially considered both types of inhibition subtractive, one possibility is that SST interneurons induce divisive inhibition during rest, such that their effect strengthens disproportionately with increasing inhibition. This may therefore account for the marked gain increase we observed in sensitizer PCs, which receive stronger SST inhibition. In principle, this prediction could also be tested by targeted recordings of identified SST→PC connections during state transitions.

What are the consequences of the enhanced gain of sensitizing PCs during locomotion? One possibility is that these changes maintain responsiveness to low contrast and transient stimuli in a visual environment that has become more dynamic with a strong component of visual flow. By selectively enhancing PCs that resist rapid depression, the circuit may preserve sensitivity to behaviourally relevant stimuli[58,82]. From a computational perspective, the ability to differentially modulate adaptive subpopulations allows the cortex to tune its operating regime to changes in behaviour. Locomotion not only modulates the synaptic and gain mechanisms we focus on here but can also enhance neural representations of visual stimuli in V1[58]. Our findings might, therefore, also be interpreted in terms of broader theories of predictive coding and attention[83]: locomotion likely reflects an internal state of heightened predictive engagement with the environment and selective amplification of sensitizing PCs could in principle support enhanced cortical representations of expected sensory features.

**Acknowledgements**

This work was supported by BBSRC grant BB/X009386/1, a PhD scholarship to SD from the Leverhulme Trust (DS-2017-011) and a Researchers at Risk Fellowship to YK from the British Academy and Council for At-Risk Academics (RaR/100503).

**Data and code availability**

All code and data reported in this paper will be shared by the lead contact upon request. Code and example data sets are available at https://github.com/lagnadoLab/CortexModel. Any additional information required to reanalyze the data reported in this manuscript is available from the lead contact upon request.

## Methods

### Animal preparation

All experimental procedures in mice were conducted according to the UK Animals Scientific Procedures Act (1986). These were performed at University of Sussex under personal and project licenses granted by the Home Office following review by the Animal Welfare and Ethics Review Board.

The animals were housed in polypropylene cages (21 cm × 35 cm) that contained nesting material, a shelter, a treadmill, a tunnel and wooden sticks. Mice were housed in groups of 2 - 3, except in some instances when reintegration into a group was unsuccessful after surgery. All animals were kept on an inverted 12-hour light-dark cycle. Results are reported from four VIP-Cre mice (VIP tm1(cre)Zjh/J Jackson #010908), fourteen SST-Cre (SST tm2.1(cre)Zjh/J, Jackson #013044), four SST-Flp (Sst tm3.1(flpo)Zjh; Jackson #028579) x VIP-Cre and ten PV-Cre (Pvalb tm1(cre)Arbr/J, Jackson #008069), all of them adult mice aged from P90 to P260 from either sex.

Mice were prepared for head-fixed multiphoton imaging through a surgical procedure in a stereotaxic frame under isoflurane anaesthesia. A titanium head plate was attached to the skull and a 3 mm craniotomy was drilled to expose the brain as described in detailed previously[9]. We then expressed AAV1.CaMKII.GCaMP6f.WPRE.SV40 to image calcium activity in pyramidal cells, AAV9.CAG.Flex.GCaMP6f.WPRE.SV40 to image interneurons in Cre lines and AAV1.EF1a-FLEX(frt)-GCaMP6f-WPRE to image SSTs in Flp lines. To excite interneurons optogenetically we used rAAV9/Syn.Flex.ChrimsonR.tdTomato and to inhibit them we used AAV5.CBA.Flex.ArchT.tdTomato.WPRE.SV40.

### Key resources table

| REAGENT or RESOURCE | SOURCE | IDENTIFIER |
|---|---|---|
| Bacterial and virus strains | | |
| AAV1 | Addgene | 100834 |
| AAV1 | Charité | VCA-222a |
| AAV5 | Addgene | 28305 |
| AAV9 | Addgene | 100835, 62723 |
| Experimental models: Organisms/strains | | |
| VIP tm1(cre)Zjh/J | Jackson | #010908 |
| SST tm2.1(cre)Zjh/J | Jackson | #013044 |
| Pvalb tm1(cre)Arbr/J | Jackson | #008069 |
| Sst tm3.1(flpo)Zjh | Jackson | #028579 |
| Recombinant DNA | | |
| AAV1.CaMKII.GCaMP6f.WPRE.SV40 | Addgene | 100834 |
| AAV9.CAG.Flex.GCaMP6f.WPRE.SV40 | Addgene | 100835 |
| AAV1.EF1a-FLEX(frt)-GCaMP6f-WPRE | Addgene | 118273 |
| rAAV9/Syn.Flex.ChrimsonR.tdTomato | Addgene | 62723 |

| | | |
|---|---|---|
| AAV5.CBA.Flex.ArchT.tdTomato.WPRE.SV40 | Addgene | 28305 |
| Software and algorithms | | |
| ScanImage | MBF Bioscience | ScanImage v.5 |
| PsychoPy | Peirce [84] | PsychoPy v. 1.82.02 |
| IgorPro | Wavemetrics | IgorPro v.8 |
| Suite2P | Pachitariu et al. [85] | MATLAB version |
| MATLAB | MathWorks, Inc | MATLAB 2021a |
| MLSpike | Deneux et al.[25] | MLSpike v.1.0 |
| V1 Model | Laboratory of Leon Lagnado | https://github.com/lagnadoLab/CortexModel |

**Multiphoton imaging *in vivo***

During imaging sessions mice were free to run on a cylindrical treadmill placed under a two-photon microscope, with stimuli being presented on two monitors covering most of the visual field. Visual stimuli were sinusoidal gratings drifting upwards (100% contrast, 1 Hz, 10 s duration) generated using the Python library PsychoPy[84]. The standard experimental protocol consisted of ten presentations of the stimulus with a 20 s interstimulus interval. When testing optogenetic manipulations these 10 trials were interleaved with 10 additional trials paired with illumination from an amber LED. The intensity of this LED was adjusted to activity of PCs to similar levels in different experiments. Running speed was measured with a rotary encoder and recorded through the imaging software (Scanimage5; Vidrio Technologies). The two-photon microscope (Scientifica SP1) employed a 16x water immersion objective (0.8 NA; Nikon) and imaging was carried out at a depth of 150-300 μm below the surface of the brain.

Raw movies were registered and segmented into regions of interest (ROIs) using the Suite2P package running in MATLAB 2021a[85] and further analysed using custom-written code in Igor Pro 8 (Wavemetrics). Here we only analyse results from the first imaging session in which the animal was exposed to the stimulus to avoid the effects of habituation observed over multiple sessions. Stimulus trials were only included for analysis if the mouse was running faster than 3 cm/s for more than 80% of the time. To calculate the response dynamics of PC, PV, SST and VIP populations we only included cells that were positively correlated with the stimulus. For each cell, the Pearson's correlation coefficients was computed between its activity trace (ΔF/F) and a stimulus trace binarized as either stimulus off (0) or stimulus on (1) using the StatsLinearCorrelationTest Function in IgorPro (Wavemetrics). The threshold for significant positive or negative correlation was set at $p < 0.05$. Measurements of adaptive properties were confined to cells which were significantly positively correlated with the stimulus. The adaptive

index (AI) was calculated from the GCaMP6f signal as AI = (R1 − R2)/(R1 + R2) where R1 is the average response over the period 0.5 - 2.5 s after stimulus onset and R2 is the average at 8-10 s.

**Estimation of firing rates**

To estimate firing rates from the recorded ΔF/F data we used the MLspike algorithm using initial parameters expected for GCaMP6f[25]. Briefly, this finds the optimal spike train to fit the calcium fluorescence trace (ΔF/F) taking into account estimates of baseline fluorescence level and neuronal parameters including the amplitude of the unitary $Ca^{2+}$ transient generated by a spike (A) and the decay time-constant of that transient (τ). These model parameters were obtained by maximum-likelihood autocalibration of ΔF/F traces, allowing conversion of relative fluorescence changes into inferred spike counts and corresponding firing rates.

In general, we followed recommendations and demos in the article and on the MLspike GitHub page. We set the range for A to be between 1 and 50% and τ was set at values from 0.05 to 3 seconds. The parameter $A_{max}$, which corresponds to the maximum amplitude of detected events, was 9, and the saturation parameter was set to 0.002. Finally, the Hill coefficient for $Ca^{2+}$ binding to GCaMP6f was varied in the range from 1 to 3.75 with step sizes of 0.25.

**Model of the circuit in layer 2/3 of V1**

We built a rate-based data-driven population model of the network circuit in the mouse visual cortex layer 2/3 (code and example data sets at https://github.com/lagnadoLab/CortexModel). The purpose of the model was to understand adaptive gain control during rest and locomoting states of four main neuron populations (PC, PV, SST, and VIP). Model parameters, both fixed and fitted, are listed in Supplementary Table 3.

The network was represented by the system of four mean-field first order ordinary differential equations (equation 1)[30]. The neuronal input-output function, $f(x)$, was a rectified power law[32]

$$f(x) = k([x]_{+}^{threshold})^{n} \qquad (6)$$

where $k$ is a scaling coefficient which was set to 1. This is a rectified linear function with a lower threshold, $[x]_{+}^{threshold}$, of zero to prevent negative values of firing rate and upper threshold of 25 to prevent run-away behaviour of the algorithm solving the network equations system. The exponent was set to n =2 but a linear activation function produced similar results during the fitting process, as observed by others[86].

Connectivity between and within populations is represented by total connection weight $w_{ji}$ which is dependent on both the number of responsive cells in the presynaptic population and the strength of individual synapses. The number of presynaptic neurons responding to the stimulus varied between rest and locomotion so to assess changes in synaptic strength caused by neuromodulators the total connection weight was divided by the number of responsive presynaptic cells (Supplementary Table 1 and equations 2 and 3 in Results). The aim of fitting the model to the average activity traces of each neuronal population was to obtain connection weights, $w_{ji}$. Weights were set to zero where published work indicated that connections are very weak or non-existent, as between SST interneurons[33,38]. The final connection weights matrix for connections within layer 2/3 was represented as:

$$W = \begin{pmatrix} w_{PC_PC} & w_{PC_PV} & w_{PC_SST} & w_{PC_VIP} \\ w_{PV_PC} & w_{PV_PV} & w_{PV_SST} & w_{PV_VIP} \\ w_{SST_PC} & w_{SST_PV} & w_{SST_SST} & w_{SST_VIP} \\ w_{VIP_PC} & w_{VIP_PV} & w_{VIP_SST} & w_{VIP_VIP} \end{pmatrix} = \begin{pmatrix} w_{PC_PC} & w_{PC_PV} & w_{PC_SST} & w_{PC_VIP} \\ w_{PV_PC} & w_{PV_PV} & 0 & 0 \\ w_{SST_PC} & w_{SST_PV} & 0 & w_{SST_VIP} \\ 0 & 0 & w_{VIP_SST} & 0 \end{pmatrix} \quad (7)$$

based on the reasonable assumption that connection probabilities are constant on the time-scale of minutes.

**External inputs driving activity**

Three types of external input drove activity in the circuit which we termed feedforward (FF), slow sensitization (SS) and feedback input (FB): the forms and origins of these are discussed in Results. These were represented in Equation 1 by the variable $In$ that was specific for each input. The FF input was defined by the following system of equations:

$$In_{FF}(t) = \begin{cases} 0, & (t < s_{start} + s_{del}) \\ I_0 + A_f e^{-(t - s_{start} - s_{del})\lambda_f}, & (s_{start} + s_{del} + s_k > t \geq s_{start} + s_{del}) \\ I_0 + A_f e^{-(t - s_{start} - s_{del})\lambda_f} + k(t - s_{start} - s_{del} - s_k), & (s_{start} + s_{dur} \geq t \geq s_{start} + s_{del} + s_k) \\ \left(I_0 + A_f e^{-(s_{dur} - s_{del})\lambda_f} + k(s_{dur} - s_{del} - s_{start})\right) e^{-(t - s_{start} - s_{dur}) decay_f}, & (t > s_{start} + s_{dur}) \end{cases} \quad (8)$$

The initial short fast-depressing component had an amplitude $A_f$ and decayed exponentially with a decay rate $\lambda_f$. The variables $s_{start}$, $s_{del}$, $s_{dur}$, $s_k$ represent stimulus start, delay in the initiation of the response in a cell, the stimulus duration and an offset after the initial peak, respectively. This offset defined the initiation of a second slow increase in feedforward input that has been observed in response to drifting gratings lasting seconds[22,44]. At the end of the stimulus presentation, experimental traces decayed relatively slowly compared with the time-constant of the model neurons and this was accounted for by including an exponentially decaying component to the input with the argument $decay_f$.

The temporal form of the feedforward input measured experimentally reflects the application of a spatio-temporal Gabor filter to a sinusoidal wave of drifting gratings[87]. This oscillation was clear in the activity of individual PCs but less evident in population averages because neurons responded with different phases, depending on the location of their receptive fields relative to the stimulus. This 1 Hz oscillation was most clearly observed in the average response of the SST population (Fig. 5C, bottom) which have larger receptive fields and therefore display less phase shifting[48]. We did not, therefore, attempt to model the oscillatory component of individual neuronal responses and concentrated on capturing the average activity across populations. The feedforward input (FF) was defined as a step of duration $s_{dur}$ with initial amplitude ($I_0$ + $A_f$) which then decayed to a steady state of $I_0$ with time-constant 210 ms, defined by fitting the initial peak of the average PC response. The steady state was half the initial maximum with $A_f = I_0$. The linear increase is a simplified representation of the sensitizing behaviour observed experimentally in layer 4 activity[22,44].

The slow sensitizing input was represented by the following system of equations:

$$In_{SS}(t) = \begin{cases} 0 & , (t < s_{start}) \\ \frac{A_s}{1+e^{(s_{start}+del-t)\lambda_s}} & , s_{start} + s_{dur} \geq t \geq s_{start}, \\ \frac{A_s e^{-(t-s_{start}-s_{dur})decay_s}}{1+e^{(del-s_{dur})\lambda_s}} & , (t > s_{start} + s_{dur}) \end{cases} \quad (9)$$

where $s_{start}$, $s_{dur}$ represent the time of the stimulus start and the stimulus duration, respectively. The slow sensitizing (SS) component is represented by a sigmoid function with an amplitude $A_s$, growth rate $\lambda_s$, and centre of sigmoid shifted to a $del$ value from the stimulus starting time. Similarly to FF, the decay phase after the stimulus end was accounted for by the argument $decay_s$.

Finally, feedback input (FB) was represented by a step function:

$$In_{FB}(t) = \begin{cases} 0, & (t < s_{start} + s_{fb_{delay}}) \cup (t > s_{start} + s_{dur}) \\ A_{fb}, & \left(s_{start} + s_{dur} \geq t \geq s_{start} + s_{fb_{delay}}\right) \\ A_{fb} e^{-(t-s_{start}-s_{dur})decay_{fb}}, & (t > s_{start} + s_{dur}) \end{cases} \quad (10)$$

where $s_{start}$, $s_{fb_delay}$, $s_{dur}$ represent time of the stimulus start, delay in the initiation of the response in a cell and the stimulus duration, respectively. The amplitude of the stimulus is defined by $A_{fb}$. Similarly to FF and SS, the decay phase after stimulus end was accounted for by the

argument $decay_{fb}$. The amplitudes of $A_{fb}$, $A_s$ and $I_o$ were fixed around 1 Hz based on the average response of PCs during locomoting state (Fig. 2).

**Fitting the model**

To obtain values of connection weights we fit the model simultaneously to the average activity traces of the four neuronal populations using the *LMFIT* library in Python[88] by minimization of reduced chi-square parameter $\chi^2$:

$$\begin{cases} \chi^2 = \sum_i^N (data_i - model_i)^2, & eps\ is\ None \\ \chi^2 = \sum_i^N \frac{(data_i - model_i)^2}{eps_i^2}, & eps\ is\ not\ None \end{cases} \quad (11)$$

Where $(data_i - model_i)$ represent an array of residuals between model and data points to be fitted, $N$ – is the number of datapoints, and $eps_i$ is the uncertainty of the data points. We weighted the data with uncertainty. We used standard errors from the locomotion and rest data.

$$\chi^2_{reduced} = \frac{\sum_i^N (data_i - model_i)^2}{stderr_i^2 (N - N_v)} = \frac{\chi^2}{(N - N_v)}, \quad (12)$$

Where $N$ is the number of data points and $N_v$ is the number of variable parameters. We set the threshold chi-square value to be 10 for locomotion and 3 for rest, given their different variabilities. An ideal "good fit" would have a value of reduced chi-square around 1, as far as uncertainty is provided[88]. We used standard errors of the mean (S.E.M) to weight the uncertainty of locomotion and rest data (eps). Additionally, to have a measure of fit quality independent of the data uncertainty and number of varied parameters we calculated root mean square error (RMSE) for each fit:

$$RMSE = \sqrt{\frac{\sum_i^N (data_i - model_i)^2}{N}}. \quad (13)$$

**Parameter Search Strategy**

Due to the high dimensionality of the parameter space, multiple parameter sets often produced similar $\chi^2_{reduced}$ values, indicating that networks with different connectivity profiles could generate similar activity patterns, which in turn made the results sensitive to the initial guess of parameters. While global optimization algorithms such as genetic algorithm and dual annealing were tested, they did not yield satisfactory performance for this model.

Instead, having access to the Artemis high performance computing cluster at Sussex University, we combined Sobol sampling[89] with local optimization methods. Sobol sampling

794 provides uniform coverage of high-dimensional parameter space. We generated 100,000 sets of
795 evenly distributed initial parameters and each Sobol-sampled parameter set was subsequently
796 refined using local optimization. We tested *Levenberg-Marquardt, Nelder-Mead, Powell* and *L-*
797 *BFGS-B* methods and noticed that *Nelder-Mead and Powell* performed across a broad parameter
798 range, whereas *Levenberg-Marquardt* and *L-BFGS-B methods* were more effective for final fine-
799 tuning. This two-stage procedure (global Sobol sampling of the initial parameters followed by local
800 optimization) allowed us to systematically explore parameter space and quantify the variability of
801 estimated connection weights. For the locomotion condition, we only obtained 37 solutions which
802 were considered good fits for having chi-square lower than 10. In order to obtain more solutions
803 for further filtering, we repeated the two-stage procedure limiting 20,000 Sobol initial conditions
804 to a subspace to average ± 2SD for each synaptic weight, rendering 9,341 good solutions without
805 changing the average and SD compared to the initial 37 solutions.
806 An important additional constraint was provided by requiring the model to fit the results of
807 optogenetic manipulations of the PV and SST populations (Fig. 4), leading to a reduced number
808 of sets of possible synaptic weights. In these experiments, the intensity of the LED was set to
809 increase or decrease PV or SST activity by a known factor between 1.6 and 2.5, as measured
810 empirically in other parallel experiments measuring GCaMP6f responses in these interneurons[9].
811 The average PV or SST activity trace was then scaled by the same factor for comparing the model
812 to observed PC activity, and RMSE value calculated for each comparison in optogenetic tests.
813 We had a total of 4 conditions: SST activation, SST inhibition, PV activation and PV inhibition
814 which we used for sequentially filtering the original group of solutions in 4 filtering steps. The
815 threshold for a good opto fitting in each step was chi-square value smaller than 0.16 and 1.2 <
816 OptoParam < 4. This approach allowed us to reduce the set of synaptic configurations, yielding
817 parameter sets that captured both the average circuit dynamics during locomotion and the
818 network's response to optogenetic perturbations.
819 For the resting state fits, we repeated the Sobol sampling and local fitting procedure using
820 the same initial steps excluding optogenetic filtering, which allowed us to estimate mean
821 parameter values and their variability (Supplementary Fig. 3). Optogenetic filtering was not
822 feasible due to the noisier nature of these traces. Alternative versions of the model were tested
823 by setting the connection weights of the tested connections to zero, this was performed with the
824 SS and FB inputs. Notably, all the resulting solutions had chi-squared values above threshold
825 indicating that slow sensitizing and feedback inputs are essential to explain circuit dynamics on
826 these time-scales (Supplementary Figure 4).
827 To assess whether model parameters segregated into distinct groups, we applied
828 unsupervised clustering using both K-means and DBSCAN algorithms. For K-means, we used
829 the Elbow method and Silhouette analysis to estimate the optimal number of clusters. We further

applied DBSCAN, estimating the neighborhood parameter (eps) from the 5th nearest neighbor distance using the KneeLocator method.

**Fitting the model to subpopulations of pyramidal cells**

The whole PC population was split into tertiles (sensitizers, intermediate cells and depressors) based on the distribution of adaptive index (Fig. 1). The average response of each subpopulation was then fit separately in for each of the good solutions from the locomoting and resting states using the two-stage fitting procedure explained above to assess changes in connectivity that describe the adaptive properties of each (Fig. 6). Three simplifying assumptions were made. First, that each subpopulation of PC receives the same shape of inputs as the average PC across the population. Second, only the synaptic weight of those connections directly targeting PCs were left free to vary while the other connections within the circuit were fixed. This was done because there is no change in activities of interneurons when separating a PC population into three subgroups and excitatory input from PCs to interneurons was taken as an average response of the whole PC population, similarly as during fitting of the whole network. Third, we used the initial conditions of the average models scaled to match amplitudes of subpopulations to average response. From Equations 1 and 6 the scaling factor is:

$$scale = \frac{w_{tertile}}{w_{avg}} = \sqrt{\frac{A_{tertile}}{A_{avg}}}, \qquad (14)$$

where $w_i$ is a weight and $A_i$ is an average amplitude of response during stimulus. Corresponding scaling multiplication factors for locomotion are: sensitizers = 1.1, intermediate = 1.2, depressors = 0.8, and for resting state are: sensitizers = 0.9, intermediate = 1.1, depressors = 0.9.

**Statistical analysis**

For the statistical tests not directly related with the model fitting we used the analytical software Igor Pro 8 and/or SPSS ('Statistical Package for the Social Sciences', IBM). To determine if the mean of one group was significantly different from another group we used a t-test (two-sided) if the distribution was normally distributed or a non-parametric Mann–Whitney U test (MWU) if it was not. We used linear mixed modelling (LMM) to test for significant interaction between locomotion state and AI tertile (Fig. 1), because cells were not paired between locomotion and resting states. Locomotion state and AI tertile were defined as fixed variables and the animal ID was defined as the random variable. All values are given as as mean ± standard error of the mean (SEM) or mean ± standard deviation (SD) as indicated in each figure legend.

# Supplementary Information

## Locomotion-dependent changes in adaptive properties of PCs

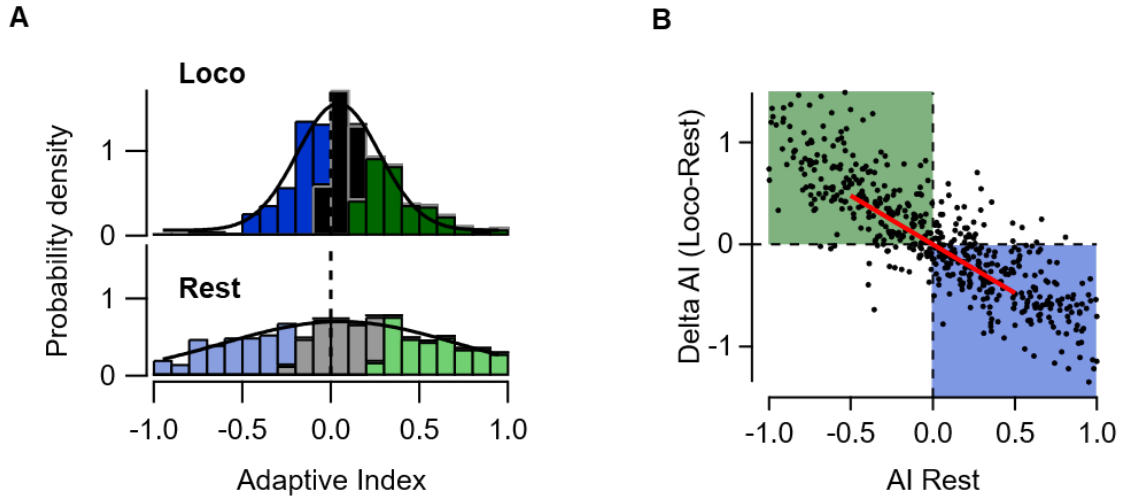


**Supplementary Figure 1. Locomotion-dependent changes in adaptive properties of PCs**

**A.** The distribution of AIs at rest and during locomotion, reproduced from Fig. 1C. **B.** Scatter plot showing the change in AI as a function of resting AI (each point a single cell; n = 522 neurons, from 9 mice). Cells that depress at rest (AI > 0) rest showed AIs closer to sensitization during locomotion (blue box in lower right quadrant) while cells that sensitize (AI < 0) showed AI closer to depression (green box in upper left quadrant). These shifts in measured AI help explaining the narrowing of the AI distribution in A. The red dashed line is fitted to the data collected from the subset of PCs with AI between -0.5 and 0.5 and reflects a correlation coefficient of r = −0.69.

## Similar time-scales of sensitizing and depressing adaptation

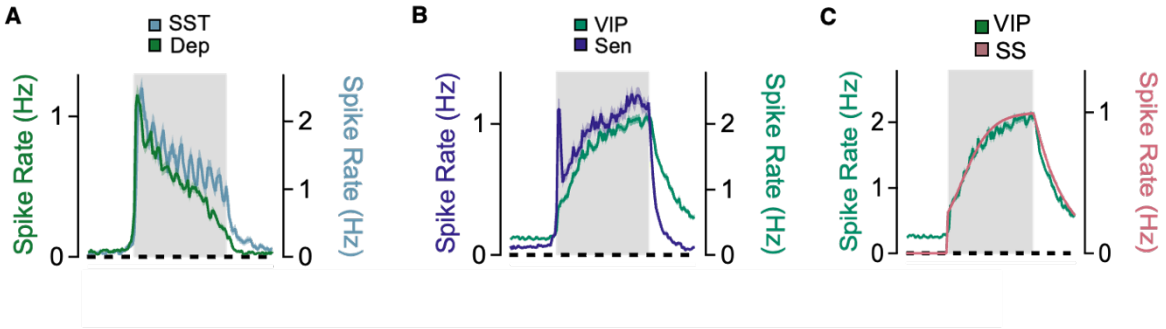


**Supplementary Figure 2. Identification of an external signal determining the time-course of slow adaptation. A.** Similar dynamics of slow depression in SSTs and the depressing tertile of PCs during locomotion. **B.** Similar dynamics of sensitization in VIPs and the sensitizing tertile of PCs (left axis, blue). **C.** The slow sensitizing input to the model (SS) was based on the average response of the VIP population during locomotion and consists of a step and sigmoid function with a time-constant = 1.71 s (see Fig. 4).

## Parameter subspace of valid solutions

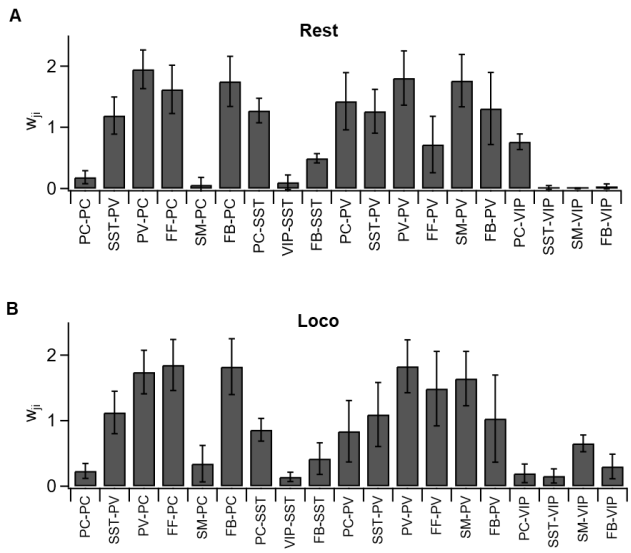


**Supplementary Figure 3. A brute force approach delimited a parameter subspace of valid solutions. A.** Average connection weights of all the solutions found in the parameter space to give a good fit for the experimental data during rest ($\chi^2_{reduced}$<3). **B.** Average connection weights of all the solutions found in the parameter space to give a good fit for the experimental data during locomotion ($\chi^2_{reduced}$<10).

**Removing external inputs impairs model performance.**

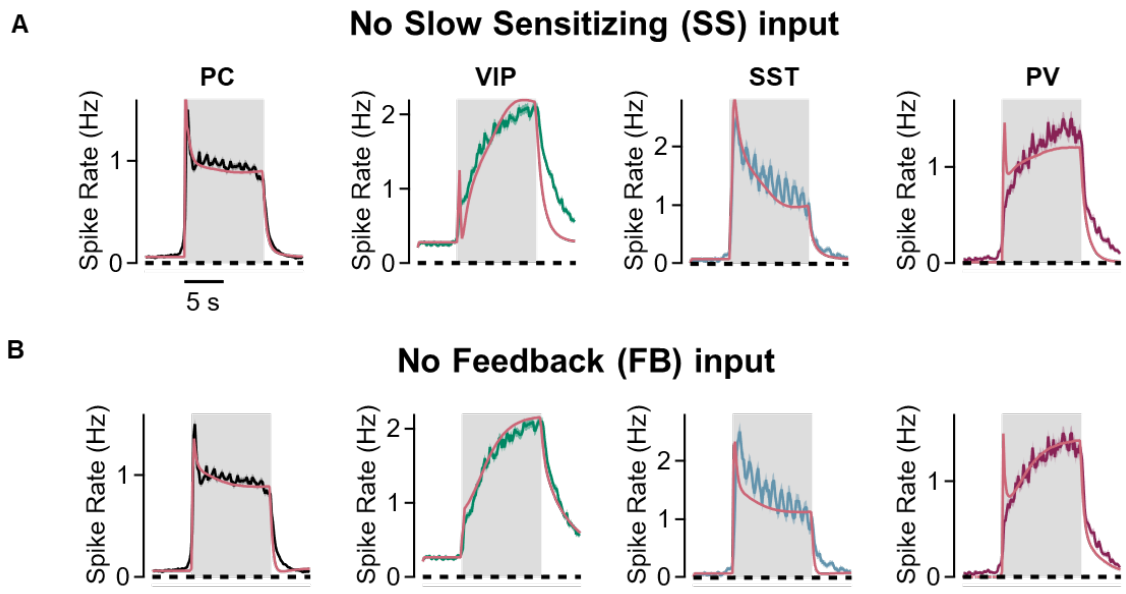


**Supplementary Figure 4. Removing external inputs impairs model performance. A.** Average firing rates of PCs (black), VIPs (green), SSTs (blue) and PVs (dark red) during stimulus presentation during locomotion and their corresponding fits from the solution with lower (RMSE = 0.14) calculated by a model without slow-sensitizing (SS) input. Note how VIP and PV dynamics are not properly captured. **B.** Same as in A for missing feedback input (FB) (RMSE = 0.14). Note how SST and PV dynamics are not properly captured.

912 **Supplementary Table 1. Locomotion-associated changes in the number of neurons**
913 **responding to the visual stimulus**
914

| Cell | Total (N, per FOV) | Rest responsive (N, per FOV) | Locomotion responsive (N, per FOV) | Rest responsive only (N, per FOV) | Relative increase during locomotion |
|---|---|---|---|---|---|
| **PC** | 78.6 ± 9.4 | 4.4 ± 1.1 | 27.8 ± 2.0*** | 0.5 ± 0.2 | 6.3 ± 1.7 |
| **SST** | 13.7 ± 1.6 | 5.1 ± 1.0 | 6.2 ± 0.7 | 0.5 ± 0.2 | 1.2 ± 0.3 |
| **PV** | 32.9 ± 5.4 | 10.1 ± 2.2 | 18.4 ± 1.6*** | 0.3 ± 0.2 | 1.8 ± 0.4 |
| **VIP** | 53.8 ± 7.2 | 11.7 ± 6.2 | 34.9 ± 3.2* | 1.3 ± 0.7 | 3.0 ± 1.6 |

915
916 From left: Total number of cells of each type imaged in a field of view (FOV) of 0.2 $mm^2$. The number of cells generating
917 a statistically significant response to the stimulus at rest (n = 11, 8, 16, 6 FOVs for PCs, SSTs, PVs and VIPs,
918 respectively) and during locomotion (n = 55, 23, 35, 22). There was a significant increase in the number of responsive
919 PCs and PVs ($p < 0.001$ in both) and VIPs ($p < 0.05$). Locomotion had no significant effect on the number of responsive
920 SSTs. Many fewer cells were responsive at rest but not locomotion, indicating that most cells responsive at rest were
921 also responsive during locomotion. Last column shows the relative change in the number of responsive neurons during
922 locomotion compared to rest.
923
924 **Supplementary Table 2. Average response amplitudes in resting and active states**
925

| | Rest (Amp in Hz) | Locomotion (Amp in Hz) | Relative Change[c] |
|---|---|---|---|
| **PC** | 0.57 | 0.96 | 0.70 |
| **SST** | 1.52 | 1.45 | -0.05 |
| **PV** | 0.93 | 1.16 | 0.25 |
| **VIP** | 0.67 | 1.63 | 1.43 |

926
927 Note that activity in external inputs were not directly measured. We therefore kept these constant
928 between rest and locomotion, so that when fitting the model changes in state were reflected only
929 in changes in their connection weights.

930 **Supplementary Table 3. List of parameters used to fit the model**

931

| Parameter (text/code)[A] | Description[B] | Value Range[C] | Type[D] | Justification/Source[E] |
|---|---|---|---|---|
| $w_{PC_PC}$ / w_0 | PC to PC population excitatory weight | Min: 0.05<br>Max: 1.0 | Fitted | Known to be less than other local weights[37-39] |
| $W_{FF_PC}$ / w_1 | Feedforward input weight to PC | Min: 0.0<br>Max: 4.0 | Fitted | |
| $W_{SS_PC}$ / w_2 | Slow sensitizing input weight to PC | Min: 0.0<br>Max: 4.0 | Fitted | |
| $W_{PV_PC}$ / w_3 | PV to PC populational inhibitory weight | Min: 0.0<br>Max: 4.0 | Fitted | |
| $W_{SST_PC}$ / w_4 | SST to PC populational inhibitory weight | Min: 0.0<br>Max: 4.0 | Fitted | |
| $W_{PC_PV}$ / w_5 | PC to PV populational excitatory weight | Min: 0.0<br>Max: 4.0 | Fitted | |
| $W_{FF_PV}$ / w_6 | Feedforward input weight to PV | Min: 0.0<br>Max: 4.0 | Fitted | |
| $W_{SS_PV}$ / w_7 | Slow sensitizing input weight to PV | Min: 0.0<br>Max: 4.0 | Fitted | |
| $W_{PV_PV}$ / w_8 | PV to PV populational inhibitory weight | Min: 0.0<br>Max: 4.0 | Fitted | |
| $W_{SST_PV}$ / w_9 | SST to PV populational inhibitory weight | Min: 0.0<br>Max: 4.0 | Fitted | |
| $W_{PC_SST}$ / w_10 | PC to SST populational excitatory weight | Min: 0.0<br>Max: 4.0 | Fitted | |
| $W_{FB_SST}$ / w_11 | Feedback input weight to SST | Min: 0.0<br>Max: 4.0 | Fitted | |
| $W_{VIP_SST}$ / w_12 | VIP to SST populational inhibitory weight | Min: 0.0<br>Max: 4.0 | Fitted | |
| $W_{PC_VIP}$ / w_13 | PC to VIP populational excitatory weight | Min: 0.0<br>Max: 4.0 | Fitted | |
| $W_{SST_VIP}$ / w_14 | SST to VIP populational inhibitory weight | Min: 0.0<br>Max: 4.0 | Fitted | |
| $W_{SS_VIP}$ / w_15 | Slow sensitizing input weight to VIP | Min: 0.0<br>Max: 4.0 | Fitted | |
| $W_{FB_PC}$ / w_16 | Feedback input weight to PC | Min: 0.0<br>Max: 4.0 | Fitted | |
| $W_{FB_PV}$ / w_17 | Feedback input weight to PV | Min: 0.0<br>Max: 4.0 | Fitted | |

| Parameter (text/code)[A] | Description[B] | Value Range[C] | Type[D] | Justification/Source[E] |
|---|---|---|---|---|
| $W_{FB_VIP}$ / w_18 | Feedback input weight to VIP | Min: 0.0<br>Max: 4.0 | Fitted | |
| $\tau_{PC}$ / τ_0 | Time constant for PCs | 15 ms | Fixed | Experimentally measured in mouse auditory cortex[90] |
| $\tau_{VIP}$ / τ_3 | Time constant for VIPs | 7.5 ms | Fixed | Experimentally measured in mouse auditory cortex[90] |
| $\tau_{PV}$ / τ_1 | Time constant for PVs | 19 ms | Fixed | Experimentally measured in mouse auditory cortex[90] |
| $\tau_{SST}$ / τ_2 | Time constant for SSTs | 19 ms | Fixed | Experimentally measured in mouse auditory cortex[90] |
| $b_{PC}$ / i_0 | Baseline activity of PC cells | Min: 0.0 Hz<br>Max: 0.7 Hz | Fitted | Constant across fittings |
| $b_{PV}$ / i_1 | Baseline activity of PV cells | Min: 0.0 Hz<br>Max: 0.7 Hz | Fitted | Constant across fittings |
| $b_{SST}$ / i_2 | Baseline activity of SST cells | Min: 0.0 Hz<br>Max: 0.7 Hz | Fitted | Constant across fittings |
| $b_{VIP}$ / i_3 | Baseline activity of VIP cells | Min: 0.0 Hz<br>Max: 0.7 Hz | Fitted | Constant across fittings |
| n / power | Exponent in input-output function (Eq. 6) | 2 | Fixed | Exponential although linear was also tested[32,86] |
| $A_f$ / ampl | Initial FF amplitude | 1 Hz | Fixed | Fitted to average PC trace |
| $I_0$ / base | FF steady-state after fast decay | 1 Hz | Fixed | Fitted to average PC trace |
| λf / decay | FF exponential decay rate | ~3.32 $s^{-1}$ (τ=301 ms) | Fixed | Fitted to average PC trace |
| $s_{del}$ (FF) / delay_1 | FF response delay | 165 ms | Fixed | Fitted to average PC trace |
| k / k | Slope of slow FF sensitization | Min: 0.005<br>Max: 0.15 | Fitted | Simplification of L4 data[22,44] |
| $s_k$ / s_start | Delay when slow FF sensitization starts | 184 ms | Fixed | To start after initial peak |
| $decay_f$ / decay_ff | FF decay time-constant after stimulus end | ~2.15 $s^{-1}$ (τ=465 ms) | Fitted | Introduced to fit tails of traces after stimulus representation |
| $A_s$ / ampl_1 | SS sigmoid amplitude | 1 Hz | Fixed | Fitted to VIP response and scaled to have average amplitude to be ~1 Hz |
| $\lambda_s$ / $\frac{1}{r_1}$ | SS sigmoid rate | ~0.58 $s^{-1}$<br>(r_1=1.71 s) | Fixed | Fitted to VIP response |
| del / delay_2 | SS sigmoid center | 1.73 s | Fixed | Fitted to VIP response |

| Parameter (text/code)[A] | Description[B] | Value Range[C] | Type[D] | Justification/Source[E] |
|---|---|---|---|---|
| $decay_s$ / decay_s | SS decay time-constant after stimulus end | ~0.27 $s^{-1}$ ($\tau$=3.7 s) | Fitted | Introduced to fit tails of traces after stimulus representation |
| $A_{fb}$ / | FB step amplitude | ~1 Hz | Fixed | Scaled to have average amplitude ~1 Hz |
| $S_{fb\ delay}$ / delay_3 | FB step delay | 370 ms | Fixed | Typical feedback latency[40]. Introduced to fit SST delay |
| $decay_{fb}$ / decay_f | FB decay time-constant after stimulus end | ~0.83 $s^{-1}$ ($\tau$=1.2 s) | Fitted | Introduced to fit tails of traces after stimulus representation |

**A**. Name of the model parameter as presented in the manuscript and in the code (text/code). **B**. Parameter purpose in the text and description. **C**. Parameter value when fixed or range where it was allowed to vary when fitted. **D**. Type of parameter value. Those parameters obtained from the litterature were Fixed, while those that were obtained to fit the data are termed Fitted. **E**. Literature source or data measure used to obtain each parameter.

## References


1. Wark, B., Lundstrom, B.N., and Fairhall, A. (2007). Sensory adaptation. Curr Opin Neurobiol *17*, 423-429. https://doi.org/10.1016/j.conb.2007.07.001.

2. Polack, P.O., Friedman, J., and Golshani, P. (2013). Cellular mechanisms of brain state-dependent gain modulation in visual cortex. Nat Neurosci *16*, 1331-1339. https://doi.org/10.1038/nn.3464.

3. Pakan, J.M., Lowe, S.C., Dylda, E., Keemink, S.W., Currie, S.P., Coutts, C.A., and Rochefort, N.L. (2016). Behavioral-state modulation of inhibition is context-dependent and cell type specific in mouse visual cortex. Elife *5*. https://doi.org/10.7554/eLife.14985.

4. McGinley, M.J., David, S.V., and McCormick, D.A. (2015). Cortical Membrane Potential Signature of Optimal States for Sensory Signal Detection. Neuron *87*, 179-192. https://doi.org/10.1016/j.neuron.2015.05.038.

5. Lin, P.A., Asinof, S.K., Edwards, N.J., and Isaacson, J.S. (2019). Arousal regulates frequency tuning in primary auditory cortex. Proc Natl Acad Sci U S A *116*, 25304-25310. https://doi.org/10.1073/pnas.1911383116.

6. Adesnik, H. (2017). Synaptic Mechanisms of Feature Coding in the Visual Cortex of Awake Mice. Neuron *95*, 1147-1159 e1144. https://doi.org/10.1016/j.neuron.2017.08.014.

7. Varela, J.A., Sen, K., Gibson, J., Fost, J., Abbott, L.F., and Nelson, S.B. (1997). A Quantitative Description of Short-Term Plasticity at Excitatory Synapses in Layer 2/3 of Rat Primary Visual Cortex. The Journal of Neuroscience *17*, 7926-7940. https://doi.org/10.1523/JNEUROSCI.17-20-07926.1997.

8. Chance, F.S., Nelson, S.B., and Abbott, L.F. (1998). Synaptic Depression and the Temporal Response Characteristics of V1 Cells. The Journal of Neuroscience *18*, 4785-4799. https://doi.org/10.1523/JNEUROSCI.18-12-04785.1998.

9. Heintz, T.G., Hinojosa, A.J., Dominiak, S.E., and Lagnado, L. (2022). Opposite forms of adaptation in mouse visual cortex are controlled by distinct inhibitory microcircuits. Nature Communications *13*, 1031. https://doi.org/10.1038/s41467-022-28635-8.

10. Niell, C.M., and Stryker, M.P. (2010). Modulation of visual responses by behavioral state in mouse visual cortex. Neuron *65*, 472-479. https://doi.org/10.1016/j.neuron.2010.01.033.

11. Fu, Y., Tucciarone, J.M., Espinosa, J.S., Sheng, N., Darcy, D.P., Nicoll, R.A., Huang, Z.J., and Stryker, M.P. (2014). A cortical circuit for gain control by behavioral state. Cell *156*, 1139-1152. https://doi.org/10.1016/j.cell.2014.01.050.

12. Dipoppa, M., Ranson, A., Krumin, M., Pachitariu, M., Carandini, M., and Harris, K.D. (2018). Vision and Locomotion Shape the Interactions between Neuron Types in Mouse Visual Cortex. Neuron *98*, 602-615.e608. https://doi.org/10.1016/j.neuron.2018.03.037.

13. Goard, M., and Dan, Y. (2009). Basal forebrain activation enhances cortical coding of natural scenes. Nat Neurosci *12*, 1444-1449. https://doi.org/10.1038/nn.2402.

14. Pronneke, A., Scheuer, B., Wagener, R.J., Mock, M., Witte, M., and Staiger, J.F. (2015). Characterizing VIP Neurons in the Barrel Cortex of VIPcre/tdTomato Mice Reveals Layer-Specific Differences. Cereb Cortex *25*, 4854-4868. https://doi.org/10.1093/cercor/bhv202.

15. Lohani, S., Moberly, A.H., Benisty, H., Landa, B., Jing, M., Li, Y., Higley, M.J., and Cardin, J.A. (2022). Spatiotemporally heterogeneous coordination of cholinergic and neocortical activity. Nat Neurosci *25*, 1706-1713. https://doi.org/10.1038/s41593-022-01202-6.

16. Kimura, F., and Baughman, R.W. (1997). Distinct muscarinic receptor subtypes suppress excitatory and inhibitory synaptic responses in cortical neurons. J Neurophysiol *77*, 709-716. https://doi.org/10.1152/jn.1997.77.2.709.

17. Hasselmo, M.E., and Bower, J.M. (1992). Cholinergic suppression specific to intrinsic not afferent fiber synapses in rat piriform (olfactory) cortex. J Neurophysiol *67*, 1222-1229. https://doi.org/10.1152/jn.1992.67.5.1222.

18. Mrzljak, L., Levey, A.I., and Goldman-Rakic, P.S. (1993). Association of m1 and m2 muscarinic receptor proteins with asymmetric synapses in the primate cerebral cortex: morphological evidence for cholinergic modulation of excitatory neurotransmission. Proc Natl Acad Sci U S A *90*, 5194-5198. https://doi.org/10.1073/pnas.90.11.5194.

19. Haider, B., Hausser, M., and Carandini, M. (2013). Inhibition dominates sensory responses in the awake cortex. Nature *493*, 97-100. https://doi.org/10.1038/nature11665.

20. Jouhanneau, J.S., Kremkow, J., Dorrn, A.L., and Poulet, J.F. (2015). In Vivo Monosynaptic Excitatory Transmission between Layer 2 Cortical Pyramidal Neurons. Cell Rep *13*, 2098-2106. https://doi.org/10.1016/j.celrep.2015.11.011.

21. Pala, A., and Petersen, C.C.H. (2015). In vivo measurement of cell-type-specific synaptic connectivity and synaptic transmission in layer 2/3 mouse barrel cortex. Neuron *85*, 68-75. https://doi.org/10.1016/j.neuron.2014.11.025.

22. Keller, A.J., Dipoppa, M., Roth, M.M., Caudill, M.S., Ingrosso, A., Miller, K.D., and Scanziani, M. (2020). A Disinhibitory Circuit for Contextual Modulation in Primary Visual Cortex. Neuron *108*, 1181-1193.e1188. https://doi.org/10.1016/j.neuron.2020.11.013.

23. Kraynyukova, N., Renner, S., Born, G., Bauer, Y., Spacek, M.A., Tushev, G., Busse, L., and Tchumatchenko, T. (2022). In vivo extracellular recordings of thalamic and cortical visual responses reveal V1 connectivity rules. Proc Natl Acad Sci U S A *119*, e2207032119. https://doi.org/10.1073/pnas.2207032119.

24. Horrocks, E.A.B., Rodrigues, F.R., and Saleem, A.B. (2024). Flexible neural population dynamics govern the speed and stability of sensory encoding in mouse visual cortex. Nat Commun *15*, 6415. https://doi.org/10.1038/s41467-024-50563-y.

25. Deneux, T., Kaszas, A., Szalay, G., Katona, G., Lakner, T., Grinvald, A., Rózsa, B., and Vanzetta, I. (2016). Accurate spike estimation from noisy calcium signals for ultrafast three-dimensional imaging of large neuronal populations in vivo. Nature Communications *7*, 12190. https://doi.org/10.1038/ncomms12190.

26. Friedrich, J., Zhou, P., and Paninski, L. (2017). Fast online deconvolution of calcium imaging data. PLoS Comput Biol *13*, e1005423. https://doi.org/10.1371/journal.pcbi.1005423.

27. Rupprecht, P., Carta, S., Hoffmann, A., Echizen, M., Blot, A., Kwan, A.C., Dan, Y., Hofer, S.B., Kitamura, K., Helmchen, F., and Friedrich, R.W. (2021). A database and deep learning toolbox for noise-optimized, generalized spike inference from calcium imaging. Nat Neurosci *24*, 1324-1337. https://doi.org/10.1038/s41593-021-00895-5.

28. Berens, P., Freeman, J., Deneux, T., Chenkov, N., McColgan, T., Speiser, A., Macke, J.H., Turaga, S.C., Mineault, P., and Rupprecht, P. (2018). Community-based benchmarking improves spike rate inference from two-photon calcium imaging data. PLoS computational biology *14*, e1006157.

29. Fairhall, A.L., Lewen, G.D., Bialek, W., and de Ruyter Van Steveninck, R.R. (2001). Efficiency and ambiguity in an adaptive neural code. Nature *412*, 787-792. https://doi.org/10.1038/35090500.

30. Wilson, H.R., and Cowan, J.D. (1972). Excitatory and Inhibitory Interactions in Localized Populations of Model Neurons. Biophysical Journal *12*, 1-24. https://doi.org/10.1016/S0006-3495(72)86068-5.

31. Miller, K.D., and Troyer, T.W. (2002). Neural Noise Can Explain Expansive, Power-Law Nonlinearities in Neural Response Functions. Journal of Neurophysiology *87*, 653-659. https://doi.org/10.1152/jn.00425.2001.

32. Rubin, Daniel B., Van Hooser, Stephen D., and Miller, Kenneth D. (2015). The Stabilized Supralinear Network: A Unifying Circuit Motif Underlying Multi-Input Integration in Sensory Cortex. Neuron *85*, 402-417. https://doi.org/10.1016/j.neuron.2014.12.026.

33. Pfeffer, C.K., Xue, M., He, M., Huang, Z.J., and Scanziani, M. (2013). Inhibition of inhibition in visual cortex: the logic of connections between molecularly distinct interneurons. Nature Neuroscience *16*, 1068-1076. https://doi.org/10.1038/nn.3446.

34. Karnani, M.M., Jackson, J., Ayzenshtat, I., Tucciarone, J., Manoocheri, K., Snider, W.G., and Yuste, R. (2016). Cooperative Subnetworks of Molecularly Similar Interneurons in Mouse Neocortex. Neuron *90*, 86-100. https://doi.org/10.1016/j.neuron.2016.02.037.

35. Brunel, N. (2000). Dynamics of sparsely connected networks of excitatory and inhibitory spiking neurons. J Comput Neurosci *8*, 183-208. https://doi.org/10.1023/a:1008925309027.

36. Deco, G., Jirsa, V.K., Robinson, P.A., Breakspear, M., and Friston, K. (2008). The dynamic brain: from spiking neurons to neural masses and cortical fields. PLoS Comput Biol *4*, e1000092. https://doi.org/10.1371/journal.pcbi.1000092.

37. Jiang, X.L., Shen, S., Cadwell, C.R., Berens, P., Sinz, F., Ecker, A.S., Patel, S., and Tolias, A.S. (2015). Principles of connectivity among morphologically defined cell types in adult neocortex. Science *350*. https://doi.org/ARTN aac9462
10.1126/science.aac9462.

38. Hage, T.A., Bosma-Moody, A., Baker, C.A., Kratz, M.B., Campagnola, L., Jarsky, T., Zeng, H., and Murphy, G.J. (2022). Synaptic connectivity to L2/3 of primary visual cortex measured by two-photon optogenetic stimulation. eLife *11*, e71103. https://doi.org/10.7554/eLife.71103.

39. Campagnola, L., Seeman, S.C., Chartrand, T., Kim, L., Hoggarth, A., Gamlin, C., Ito, S., Trinh, J., Davoudian, P., Radaelli, C., et al. (2022). Local connectivity and synaptic dynamics in mouse and human neocortex. Science *375*, eabj5861. https://doi.org/10.1126/science.abj5861.

40. Oh, S.W., Harris, J.A., Ng, L., Winslow, B., Cain, N., Mihalas, S., Wang, Q., Lau, C., Kuan, L., Henry, A.M., et al. (2014). A mesoscale connectome of the mouse brain. Nature *508*, 207-214. https://doi.org/10.1038/nature13186.

41. Froudarakis, E., Fahey, P.G., Reimer, J., Smirnakis, S.M., Tehovnik, E.J., and Tolias, A.S. (2019). The Visual Cortex in Context. Annu Rev Vis Sci *5*, 317-339. https://doi.org/10.1146/annurev-vision-091517-034407.

42. Roelfsema, P.R., Lamme, V.A., and Spekreijse, H. (1998). Object-based attention in the primary visual cortex of the macaque monkey. Nature *395*, 376-381. https://doi.org/10.1038/26475.

43. Leinweber, M., Ward, D.R., Sobczak, J.M., Attinger, A., and Keller, G.B. (2017). A Sensorimotor Circuit in Mouse Cortex for Visual Flow Predictions. Neuron *96*, 1204. https://doi.org/10.1016/j.neuron.2017.11.009.

44. Makino, H., and Komiyama, T. (2015). Learning enhances the relative impact of top-down processing in the visual cortex. Nature Neuroscience *18*, 1116-1122. https://doi.org/10.1038/nn.4061.

45. Fiser, A., Mahringer, D., Oyibo, H.K., Petersen, A.V., Leinweber, M., and Keller, G.B. (2016). Experience-dependent spatial expectations in mouse visual cortex. Nat Neurosci *19*, 1658-1664. https://doi.org/10.1038/nn.4385.

46. Zhang, S., Xu, M., Kamigaki, T., Hoang Do, J.P., Chang, W.-C., Jenvay, S., Miyamichi, K., Luo, L., and Dan, Y. (2014). Long-range and local circuits for top-down modulation of visual cortex processing. Science *345*, 660-665. https://doi.org/doi:10.1126/science.1254126.

47. Jin, M., and Glickfeld, L.L. (2020). Mouse Higher Visual Areas Provide Both Distributed and Specialized Contributions to Visually Guided Behaviors. Curr Biol *30*, 4682-4692.e4687. https://doi.org/10.1016/j.cub.2020.09.015.

48. Adesnik, H., Bruns, W., Taniguchi, H., Huang, Z.J., and Scanziani, M. (2012). A neural circuit for spatial summation in visual cortex. Nature *490*, 226-231. https://doi.org/10.1038/nature11526.

49. Keller, G.B., and Mrsic-Flogel, T.D. (2018). Predictive Processing: A Canonical Cortical Computation. Neuron *100*, 424-435. https://doi.org/https://doi.org/10.1016/j.neuron.2018.10.003.

50. Shen, S., Jiang, X., Scala, F., Fu, J., Fahey, P., Kobak, D., Tan, Z., Zhou, N., Reimer, J., Sinz, F., and Tolias, A.S. (2022). Distinct organization of two cortico-cortical feedback pathways. Nat Commun *13*, 6389. https://doi.org/10.1038/s41467-022-33883-9.

51. Liu, Y., Zhang, J., Jiang, Z., Qin, M., Xu, M., Zhang, S., and Ma, G. (2024). Organization of corticocortical and thalamocortical top-down inputs in the primary visual cortex. Nat Commun *15*, 4495. https://doi.org/10.1038/s41467-024-48924-8.

52. Jordan, R., and Keller, G.B. (2020). Opposing Influence of Top-down and Bottom-up Input on Excitatory Layer 2/3 Neurons in Mouse Primary Visual Cortex. Neuron *108*, 1194-1206.e1195. https://doi.org/10.1016/j.neuron.2020.09.024.

53. Zhang, S., Xu, M., Kamigaki, T., Hoang Do, J.P., Chang, W.C., Jenvay, S., Miyamichi, K., Luo, L., and Dan, Y. (2014). Selective attention. Long-range and local circuits for top-down modulation of visual cortex processing. Science *345*, 660-665. https://doi.org/10.1126/science.1254126.

54. Yogesh, B., and Keller, G.B. (2024). Cholinergic input to mouse visual cortex signals a movement state and acutely enhances layer 5 responsiveness. Elife *12*. https://doi.org/10.7554/eLife.89986.

55. Kim, E.J., Jacobs, M.W., Ito-Cole, T., and Callaway, E.M. (2016). Improved Monosynaptic Neural Circuit Tracing Using Engineered Rabies Virus Glycoproteins. Cell Rep *15*, 692-699. https://doi.org/10.1016/j.celrep.2016.03.067.

56. Tennoe, S., Halnes, G., and Einevoll, G.T. (2018). Uncertainpy: A Python Toolbox for Uncertainty Quantification and Sensitivity Analysis in Computational Neuroscience. Front Neuroinform *12*, 49. https://doi.org/10.3389/fninf.2018.00049.

57. Billeh, Y.N., Cai, B., Gratiy, S.L., Dai, K., Iyer, R., Gouwens, N.W., Abbasi-Asl, R., Jia, X., Siegle, J.H., Olsen, S.R., et al. (2020). Systematic Integration of Structural and Functional Data into Multi-scale Models of Mouse Primary Visual Cortex. Neuron *106*, 388-403 e318. https://doi.org/10.1016/j.neuron.2020.01.040.

58. Dadarlat, M.C., and Stryker, M.P. (2017). Locomotion Enhances Neural Encoding of Visual Stimuli in Mouse V1. J Neurosci *37*, 3764-3775. https://doi.org/10.1523/JNEUROSCI.2728-16.2017.

59. Erisken, S., Vaiceliunaite, A., Jurjut, O., Fiorini, M., Katzner, S., and Busse, L. (2014). Effects of Locomotion Extend throughout the Mouse Early Visual System. Current Biology *24*, 2899-2907. https://doi.org/10.1016/j.cub.2014.10.045.

60. Wilson, N.R., Runyan, C.A., Wang, F.L., and Sur, M. (2012). Division and subtraction by distinct cortical inhibitory networks in vivo. Nature *488*, 343-348. https://doi.org/10.1038/nature11347.

61. Lee, S.-H., Kwan, A.C., Zhang, S., Phoumthipphavong, V., Flannery, J.G., Masmanidis, S.C., Taniguchi, H., Huang, Z.J., Zhang, F., Boyden, E.S., et al. (2012). Activation of specific interneurons improves V1 feature selectivity and visual perception. Nature *488*, 379-383. https://doi.org/10.1038/nature11312.

1115 62. Phillips, E.A., and Hasenstaub, A.R. (2016). Asymmetric effects of activating and inactivating cortical
1116 interneurons. Elife *5*. https://doi.org/10.7554/eLife.18383.

1117 63. Pi, H.-J., Hangya, B., Kvitsiani, D., Sanders, J.I., Huang, Z.J., and Kepecs, A. (2013). Cortical
1118 interneurons that specialize in disinhibitory control. Nature *503*, 521-524.
1119 https://doi.org/10.1038/nature12676.

1120 64. Glickfeld, L.L., Andermann, M.L., Bonin, V., and Reid, R.C. (2013). Cortico-cortical projections in
1121 mouse visual cortex are functionally target specific. Nat Neurosci *16*, 219-226.
1122 https://doi.org/10.1038/nn.3300.

1123 65. Han, Y., Kebschull, J.M., Campbell, R.A.A., Cowan, D., Imhof, F., Zador, A.M., and Mrsic-Flogel, T.D.
1124 (2018). The logic of single-cell projections from visual cortex. Nature *556*, 51-56.
1125 https://doi.org/10.1038/nature26159.

1126 66. Ballinger, E.C., Ananth, M., Talmage, D.A., and Role, L.W. (2016). Basal Forebrain Cholinergic Circuits
1127 and Signaling in Cognition and Cognitive Decline. Neuron *91*, 1199-1218.
1128 https://doi.org/10.1016/j.neuron.2016.09.006.

1129 67. Munoz, W., and Rudy, B. (2014). Spatiotemporal specificity in cholinergic control of neocortical
1130 function. Curr Opin Neurobiol *26*, 149-160. https://doi.org/10.1016/j.conb.2014.02.015.

1131 68. Gil, Z., Connors, B.W., and Amitai, Y. (1997). Differential regulation of neocortical synapses by
1132 neuromodulators and activity. Neuron *19*, 679-686. https://doi.org/10.1016/s0896-6273(00)80380-3.

1133 69. Xiang, Z., Huguenard, J.R., and Prince, D.A. (1998). GABAA receptor-mediated currents in
1134 interneurons and pyramidal cells of rat visual cortex. J Physiol *506 ( Pt 3)*, 715-730.
1135 https://doi.org/10.1111/j.1469-7793.1998.715bv.x.

1136 70. Kruglikov, I., and Rudy, B. (2008). Perisomatic GABA release and thalamocortical integration onto
1137 neocortical excitatory cells are regulated by neuromodulators. Neuron *58*, 911-924.
1138 https://doi.org/10.1016/j.neuron.2008.04.024.

1139 71. Urban-Ciecko, J., and Barth, A.L. (2016). Somatostatin-expressing neurons in cortical networks. Nat
1140 Rev Neurosci *17*, 401-409. https://doi.org/10.1038/nrn.2016.53.

1141 72. Chen, N., Sugihara, H., and Sur, M. (2015). An acetylcholine-activated microcircuit drives temporal
1142 dynamics of cortical activity. Nat Neurosci *18*, 892-902. https://doi.org/10.1038/nn.4002.

1143 73. Wang, Y., Gupta, A., Toledo-Rodriguez, M., Wu, C.Z., and Markram, H. (2002). Anatomical,
1144 physiological, molecular and circuit properties of nest basket cells in the developing somatosensory
1145 cortex. Cereb Cortex *12*, 395-410. https://doi.org/10.1093/cercor/12.4.395.

1146 74. Silberberg, G., and Markram, H. (2007). Disynaptic inhibition between neocortical pyramidal cells
1147 mediated by Martinotti cells. Neuron *53*, 735-746. https://doi.org/10.1016/j.neuron.2007.02.012.

1148 75. Muñoz, W., Tremblay, R., Levenstein, D., and Rudy, B. (2017). Layer-specific modulation of
1149 neocortical dendritic inhibition during active wakefulness. Science *355*, 954-959.

1150 76. Tremblay, R., Lee, S., and Rudy, B. (2016). GABAergic Interneurons in the Neocortex: From Cellular
1151 Properties to Circuits. Neuron *91*, 260-292. https://doi.org/10.1016/j.neuron.2016.06.033.

1152 77. Atallah, B.V., Bruns, W., Carandini, M., and Scanziani, M. (2012). Parvalbumin-expressing
1153 interneurons linearly transform cortical responses to visual stimuli. Neuron *73*, 159-170.
1154 https://doi.org/10.1016/j.neuron.2011.12.013.

1155 78. Fino, E., and Yuste, R. (2011). Dense Inhibitory Connectivity in Neocortex. Neuron *69*, 1188-1203.
1156 https://doi.org/https://doi.org/10.1016/j.neuron.2011.02.025.

79. Hofer, S.B., Ko, H., Pichler, B., Vogelstein, J., Ros, H., Zeng, H., Lein, E., Lesica, N.A., and Mrsic-Flogel, T.D. (2011). Differential connectivity and response dynamics of excitatory and inhibitory neurons in visual cortex. Nature neuroscience *14*, 1045-1052.

80. Rodarie, D., Verasztó, C., Roussel, Y., Reimann, M., Keller, D., Ramaswamy, S., Markram, H., and Gewaltig, M.-O. (2022). A method to estimate the cellular composition of the mouse brain from heterogeneous datasets. PLOS Computational Biology *18*, e1010739.

81. Schneider-Mizell, C.M., Bodor, A.L., Brittain, D., Buchanan, J., Bumbarger, D.J., Elabbady, L., Gamlin, C., Kapner, D., Kinn, S., Mahalingam, G., et al. (2024). Cell-type-specific inhibitory circuitry from a connectomic census of mouse visual cortex. bioRxiv. https://doi.org/10.1101/2023.01.23.525290.

82. Bennett, C., Arroyo, S., and Hestrin, S. (2013). Subthreshold mechanisms underlying state-dependent modulation of visual responses. Neuron *80*, 350-357. https://doi.org/10.1016/j.neuron.2013.08.007.

83. Rao, R.P., and Ballard, D.H. (1999). Predictive coding in the visual cortex: a functional interpretation of some extra-classical receptive-field effects. Nat Neurosci *2*, 79-87. https://doi.org/10.1038/4580.

84. Peirce, J.W. (2007). PsychoPy--Psychophysics software in Python. J Neurosci Methods *162*, 8-13. https://doi.org/10.1016/j.jneumeth.2006.11.017.

85. Pachitariu, M., Stringer, C., Schröder, S., Dipoppa, M., Rossi, L.F., Carandini, M., and Harris, K.D. (2016). Suite2p: beyond 10,000 neurons with standard two-photon microscopy. bioRxiv.

86. Kuchibhotla, K.V., Gill, J.V., Lindsay, G.W., Papadoyannis, E.S., Field, R.E., Sten, T.A.H., Miller, K.D., and Froemke, R.C. (2017). Parallel processing by cortical inhibition enables context-dependent behavior. Nature Neuroscience *20*, 62-71. https://doi.org/10.1038/nn.4436.

87. Gáspár, M.E., Polack, P.-O., Golshani, P., Lengyel, M., and Orbán, G. (2019). Representational untangling by the firing rate nonlinearity in V1 simple cells. eLife *8*, e43625. https://doi.org/10.7554/eLife.43625.

88. Newville, M., Stensitzki, T., Allen, D.B., and Ingargiola, A. (2014). LMFIT: Non-Linear Least-Square Minimization and Curve-Fitting for Python (Zenodo).

89. Sobol, I.M., and Y. L. Levitan (1976). The production of points uniformly distributed in a multidimensional. Technical Report Preprint *40*.

90. Seay, M.J., Natan, R.G., Geffen, M.N., and Buonomano, D.V. (2020). Differential Short-Term Plasticity of PV and SST Neurons Accounts for Adaptation and Facilitation of Cortical Neurons to Auditory Tones. J Neurosci *40*, 9224-9235. https://doi.org/10.1523/JNEUROSCI.0686-20.2020.